

1 **Modelling high-frequency seismograms at ocean bottom seismometers:**
2 **effects of heterogeneous structures on source parameter estimation for**
3 **small offshore earthquakes and shallow low-frequency tremors**

4 **Authors**

5 **Shunsuke TAKEMURA^{1*}, Suguru YABE², Kentaro EMOTO³**

6 ¹**Earthquake Research Institute, the University of Tokyo, 1-1-1 Yayoi, Bunkyo-ku,**
7 **Tokyo, 113-0032, Japan**

8 ²**Geological Survey of Japan, National Institute of Advanced Industrial Science and**
9 **Technology, Tsukuba Central 7, 1-1-1 Higashi, Tsukuba, Ibaraki, 305-8567, Japan**

10 ³**Geophysics, Graduate School of Science, Tohoku University, 6-3, Aramaki-aza-**
11 **aoba, Aoba-ku, Sendai, 980-8578, Japan**

12

13 **Running Title**

14 Modelling HF seismograms at OBSs

15 **Corresponding Author**

16 Shunsuke Takemura

17 E-mail: shunsuke@eri.u-tokyo.ac.jp

18 Phone: +81 3-5841-5689

19

20 **Summary**

21 The source characteristics of offshore seismic events, especially interplate regular (or fast)
22 and slow earthquakes, provide key information on their source physics and frictional
23 conditions at the plate boundary. Due to strong three-dimensional heterogeneities in offshore
24 regions, such as those relating to seawater, accretionary prism, and small-scale velocity
25 heterogeneity, conventional methods using a one-dimensional Earth model may misestimate
26 source parameters such as duration and radiation energy. Estimations could become severely
27 inaccurate for small offshore seismic events because high-frequency (> 1 Hz) seismograms,
28 which are strongly affected by three-dimensional heterogeneities, are only available for
29 analysis due to their signal-to-noise ratio. To investigate the effects of offshore
30 heterogeneities on source parameter estimation for small seismic events, we analyse observed
31 and simulated high-frequency seismograms southeast off the Kii Peninsula, Japan, in the
32 Nankai subduction zone. Numerical simulations of seismic wave propagation using a three-
33 dimensional velocity structure model clarify the effects of each heterogeneity. Comparisons
34 between observations and model simulations demonstrate that the thick low-velocity
35 accretionary prism has significant effects on high-frequency seismic wave propagation.
36 Especially for shallow low-frequency tremors occurring at depths just below the accretionary
37 prism toe, seismogram durations are significantly broader than an assumed source duration,
38 even for stations with epicentral distances of approximately 10 km. Spindle-shape
39 seismogram envelopes are observed even at such close stations. Our results suggest that
40 incorporating three-dimensional heterogeneities is necessary for practical estimation of
41 source parameters for small offshore events.

42 **Keywords:**

43 Computational seismology, earthquake ground motions, earthquake source observations,
44 seismicity and tectonics, wave propagation, wave scattering and diffraction

45

46 **1. Introduction**

47 To understand the physics and characteristics of earthquake sources, seismologists analyse
48 observed seismograms in the world. Following correction of the frequency responses of
49 seismometers and local site effects at each station, the observed seismograms provide
50 information on source rupture complexity and heterogeneous structures along each
51 propagation path. For centroid moment tensor (CMT) inversion for teleseismic events or
52 local crustal earthquakes using low-frequency (< 0.1 Hz) seismograms, path effects are
53 typically evaluated by assuming a simple one-dimensional (1D) Earth model (e.g., Ekström et
54 al., 2012; Kanamori & Rivera, 2008; Nakano et al., 2008) because low-frequency seismic
55 waves are usually considered insensitive to structural heterogeneities. By developments of
56 computer resources and three-dimensional (3D) subsurface structure models, the CMT
57 inversions using 3D velocity models have been practically conducted not only crustal but also
58 offshore earthquakes (e.g., Hejrani et al. 2017; Takemura, Okuwaki, et al. 2019; Wang &
59 Zhan 2020). The 3D heterogeneities in the offshore regions, such as seawater, accretionary
60 prism, and small-scale velocity heterogeneity, are developed just beneath the epicentre
61 regions of offshore subduction zone earthquakes. Thus, the 3D CMT method better constrains
62 earthquake source characteristics compared to the 1D method, especially for offshore
63 earthquakes.

64 Moment tensor inversion is only applicable to moderate-to-large earthquakes, due to
65 signal-to-noise ratios of coherent low-frequency seismic signals. Thus, small events, such as
66 microearthquakes or tectonic and volcanic tremors, are usually evaluated via methods based
67 on the amplitudes or energies of high-frequency (> 1 Hz) seismic waves (e.g., Fletcher &
68 McGarr, 2011; Gusev & Pavlov, 1991; Maeda & Obara, 2009; Nakahara, 2008; Poiata et al.,
69 2018; Sawazaki & Enescu, 2014; Staudenmaier et al., 2016). The precise evaluation of small
70 events is important for not only understanding source physics (e.g., Ellsworth & Bulut, 2018;
71 Gomberg et al., 2016; Hawthorne et al., 2019; Ide et al., 2003; Supino et al., 2020; Thomas et
72 al., 2016; Uchide & Ide, 2010) but also for monitoring crustal and volcanic activities (e.g.,
73 Battaglia & Aki, 2003; Kato et al., 2012; Kumagai et al., 2013; Kurokawa et al., 2016; Peng
74 & Zhao, 2009; Yabe & Ide, 2014). The characteristics of high-frequency seismic waves, and
75 related small-scale structural properties in onshore regions, have been widely investigated by
76 numerical, theoretical and observational approaches (e.g., Carcolé & Sato 2010; Chaput et al.
77 2015; Margerin 2005; Morioka et al. 2017; Saito et al. 2002,; Takahashi et al. 2009;
78 Takemura et al. 2016, 2017; Wegler et al. 2006). Consequently, estimated location and energy

79 for onshore small seismic events are generally robust even with 1D conventional methods.

80 Due to long distances between onshore stations and offshore seismic sources, the source
81 parameters of small offshore seismic events cannot be precisely determined from onshore
82 seismic stations. Thus, temporal observations of ocean bottom seismometers (OBSs) have
83 been extensively carried out. Around the Japanese Islands, permanent OBS networks of
84 DONET and S-net (National Research Institute for Earth Science and Disaster Resilience,
85 2019c, 2019a) have been recently deployed. Several studies have used temporal OBS data or
86 such permanent networks to estimate the source characteristics of small earthquakes and
87 shallow low-frequency tremors (LFTs) (e.g., Nakano et al., 2015, 2019; Nishikawa et al.,
88 2019; Tamaribuchi et al., 2019; Tanaka et al., 2019; Yabe et al., 2019). Offshore 3D
89 heterogeneities significantly affect seismic wave propagation even for low-frequency ground
90 motions (e.g., Gomberg 2018; Guo et al. 2016; Nakamura et al. 2015; Shapiro et al. 1998,
91 Takemura, Kubo, et al. 2019; Volk et al. 2017) yet 1D velocity structure models have been
92 widely used in these analyses, potentially providing incorrect estimations of source
93 parameters, especially for duration and source energy.

94 Figure 1 shows examples of NS-component filtered velocity seismograms of onshore F-
95 net and offshore DONET stations (National Research Institute for Earth Science and Disaster
96 Resilience, 2019b, 2019a). The estimated event sizes of regular earthquakes in Figure 1 were
97 similar. The event size of a shallow LFT, estimated using an accompanied shallow very low-
98 frequency earthquake (VLFE), was also similar. However, the observed waveforms of these
99 events were very different. Although an F-net seismogram of an onshore regular earthquake
100 showed a short-duration pulse-like *S*-wave envelope, a DONET seismogram of an offshore
101 regular earthquake was broadened due to multiple wave packets. A seismogram of a shallow
102 LFT was more complex, showing a spindle-shaped seismogram envelope. In order to
103 understand differences in source processes among these seismic events, it is necessary to
104 evaluate the effects of seismic wave propagation through 3D strong heterogeneities in
105 offshore regions, including seawater, low-velocity accretionary prism, and small-scale
106 velocity heterogeneity.

107 In this study, to investigate the effects of offshore heterogeneities on high-frequency
108 seismic waves and source parameter estimations, we analyse simulated and observed high-
109 frequency seismograms at offshore seismic stations. Using a realistic 3D offshore
110 heterogeneous model, we conduct 3D numerical simulations of seismic wave propagation via
111 open-source finite-difference method (FDM) software. Simulated seismograms enable

112 analysis of the effects of each heterogeneity on offshore high-frequency seismograms. By
113 combining various structural model simulations and observed seismograms, we can evaluate
114 the effects of seawater, accretionary prism, and small-scale velocity heterogeneity on high-
115 frequency seismograms at offshore stations. We also estimated a source time function (STF)
116 of a shallow LFT via the conventional method, and conducted a numerical simulation of
117 seismic wave propagation using the estimated STF. By comparing simulated and observed
118 seismogram envelope shapes, we also discuss reliable settings for source parameter
119 estimations of offshore small seismic events via conventional methods.

120 **2. Data and Methods**

121 The target region, southeast off the Kii Peninsula, southwest Japan (Figures 1 and 2a), has
122 repeatedly experienced large megathrust earthquakes (e.g., Ando, 1975). To understand stress
123 and frictional conditions of the megathrust zone along the Nankai Trough, regular and slow
124 earthquakes around this region have been monitored by DONET stations (locations
125 represented by diamond symbols in Figures 1 and 2a), operated jointly by the Japan Agency
126 for Marine-Earth Science and Technology (JAMSTEC) and the National Research Institute
127 for Earth Science and Disaster Resilience (NIED). Various small seismic phenomena,
128 including small interplate and intraplate regular earthquakes and shallow slow earthquakes,
129 have been observed by broadband seismometers installed at each DONET station. Interplate
130 earthquake activity is quite low, except for activity of the 2016 southeast off Kii Peninsula
131 earthquake (Nakano, Hyodo, et al., 2018; Wallace et al., 2016), but shallow slow earthquakes
132 are often observed (e.g., Annoura et al., 2017; Araki et al., 2017; Nakano, Hori, et al., 2018;
133 Toh et al., 2018). Precise source parameter estimation of such small phenomena is an
134 important issue for understanding earthquake source physics and seismic activity in the
135 Nankai subduction zone.

136 The effects of offshore heterogeneities on seismic wave propagation were investigated
137 using both simulated seismograms and three-component broadband velocity seismograms of
138 DONET stations. Simulated seismograms were evaluated at the same locations as the
139 observational stations and virtual seafloor seismic stations, which were uniformly distributed
140 at a horizontal interval of 0.05° in the model region. We used parallel FDM code of
141 OpenSWPC software (Maeda et al., 2017) to simulate seismic wave propagation of a shallow
142 LFT, and small regular earthquakes in the 3D viscoelastic medium. To avoid artificial
143 reflections from model boundaries, perfectly matched layer boundary conditions (e.g., Zhang
144 & Shen, 2010) were assumed at each model boundary.

145 The 3D velocity structure model developed by Koketsu *et al.* (2012) was used as the
146 model beneath the bedrock. This model has been widely used for various applications across
147 Japan (e.g., Furumura & Kennett 2018; Iwaki *et al.* 2018; Petukhin *et al.* 2016; Takemura *et*
148 *al.* 2017; Takemura, Okuwaki, *et al.* 2019). The ETOPO1 model (Amante & Eakins, 2009)
149 was used as the topographic model in simulations. The 1D *S*-wave velocity structures beneath
150 the DONET stations (Tonegawa *et al.*, 2017) were used to model a 3D velocity structure
151 within the accretionary prism. Extrapolation and interpolation of 1D local *S*-wave velocity
152 structures via the ‘*Surface*’ gridding algorithm of the Generic Mapping Tools (Wessel *et al.*,
153 2013) were applied to construct the 3D accretionary prism model. Details of the model
154 construction are described in the Supporting Material (Text S1). The *P*- and *S*-wave
155 velocities, density (V_P , V_S , and ρ) and attenuations (Q_P and Q_S) for each layer are listed in
156 Table 1. The minimum V_S of 0.5 km/s was assumed in the solid column. The 3D simulation
157 model for shallow LFT and small earthquakes covered an area of $120 \times 82.5 \times 45 \text{ km}^3$
158 (delineated by the dashed-blue rectangle in Figure 2a), which was discretised by a grid
159 interval of 0.015 km. Cross-sections of the constructed layered structure model are illustrated
160 in Figures 2b and 2c. This model is the reference model. Simulations of high-frequency
161 seismic wave propagation were conducted using calculation resources of the Earth Simulator
162 at JAMSTEC. Each simulation requires 24 TB of computer memory and a wall-clock time of
163 6.3 hr by parallel computing using 1,280 nodes (5,120 cores) of the Earth Simulator to
164 evaluate seismic wave propagation of 60 s.

165 According to the observed seismic activity in this region, shallow LFT, regular interplate
166 and intraslab earthquakes were considered in our simulations (Table 2). Events A, B and C
167 occurred on 16 April 2016, 19 April 2016 and 4 December 2014, respectively. Because
168 source parameters for events A—C were not precisely estimated, we assumed double-couple
169 point sources of CMT solutions for the nearest shallow VLFE or moderate size earthquakes
170 (Takemura, Okuwaki, *et al.* 2019; Takemura *et al.* 2019). Although source durations of LFTs
171 estimated in previous studies range from 10 to 30 s (e.g., Gomberg *et al.*, 2016; Nakano *et al.*,
172 2019; Yabe *et al.*, 2019), the present source models all employed a simple triangle function of
173 duration 0.2 s for investigating the characteristics of seismic wave propagation.

174 **3. Simulation results**

175 Figure 3 shows snapshots of the simulated *P*- and *S*-wave propagations of a shallow LFT.
176 The *P*- and *S*-wavefields were evaluated by calculating the divergence and rotation,
177 respectively, of the simulated velocity wavefield of a shallow LFT source. The *P* and *S*

178 waves, which radiated from a shallow LFT on the plate boundary, showed complex
179 propagation through heterogeneous structures and repeating scattering and reflection from
180 each layer boundary. The intensities of *P* and *S* waves at depths below the bedrock were very
181 weak, but large seismic energies were trapped within the low-velocity accretionary prism.
182 The *P* waves were also trapped within the seawater layer as ocean acoustic waves. According
183 to these simulated *P* and *S* wavefields, long-duration complicated simulated seismograms are
184 expected.

185 The root-mean-square (RMS) envelopes for the shallow LFT simulation are shown in
186 Figure 4a. The RMS envelopes were evaluated by the sum of three-component envelopes for
187 frequencies of 1–5 Hz. Because the FDM to evaluate seismic wave propagation for
188 frequencies less than 5 Hz due to our simulation settings, we investigated simulated
189 seismograms for the 1–5 Hz frequency band, which is lower than the typical dominant
190 frequencies of LFTs (2–8 Hz). After calculating vector sum of three-component envelopes, a
191 moving average with a time window of 1 s was applied. Each trace was normalized by each
192 maximum amplitude. The envelopes at stations around the epicentre (< 10 km) clearly show
193 short-duration *S*-wave pulse and weak later phases. However, as distance increased, RMS
194 envelopes were rapidly broadened. At distances greater than 30 km the onsets of *S* waves
195 were not clear and RMS envelopes were characterized by spindle shapes with durations of
196 20–30 s. These *S*-wave durations were significantly longer than the assumed source pulse
197 (0.2 s). This broadening and delayed peak of simulated seismogram envelopes is much larger
198 than for seismic waves propagating through typical lithosphere (e.g., Saito et al., 2005;
199 Takahashi et al., 2007; Tripathi et al., 2010)

200 On the other hand, the simulated RMS envelopes for regular earthquakes were composed
201 of pulse-like *S* waves and multiple distinct later packets (Figures 4b and 4c). Multiple later
202 packets may be developed by the seawater layer, accretionary prism or subducting oceanic
203 plate. The simulation of the deepest source (event C; Figure 4c) shows simpler RMS
204 envelopes. Simulations of all events were conducted using the same source time function
205 (0.2 s triangle function), but the simulated envelopes for event A were very different from
206 those for events B and C. Significant differences were found in simulated RMS envelopes
207 between events A and B, despite similar source mechanisms, both of which are low-angle
208 thrust faulting on the plate boundary. Thus, we considered that differences in simulated RMS
209 envelopes between a shallow LFT and regular earthquakes could be caused by shallower
210 heterogeneous structures.

211 Figure 5 shows observed RMS envelopes of a shallow LFT on 16 April 2016, an interplate
212 earthquake on 19 April 2016 and an intraplate earthquake on 4 December 2014. Because we
213 did not know the precise source parameters of these small events and incorporate the effects
214 of site amplification at each station, we compared the shapes of seismogram envelopes
215 between simulations (Figure 4) and observations (Figure 5). Similar characteristics of
216 simulated RMS envelopes were found in observations. Although the durations of observed
217 RMS envelopes for a shallow LFT were longer than the simulation with a 0.2 s triangle
218 function (Figure 4 a), the observed RMS envelopes also broadened with increasing distance
219 (Figure 5a). Pulse-like wave packets of *S* waves and later phases appeared in observed RMS
220 envelopes for regular earthquakes (Figures 5b and 5c). The similarity of RMS envelopes
221 between simulations and observations suggest that our local 3D model reliably characterizes
222 seismic wave propagation southeast off the Kii Peninsula, Japan.

223 Figure 6 shows the spatial variations of maximum RMS amplitudes and envelope half-
224 value widths derived from ground motion simulation for a shallow LFT. The envelope half-
225 value width is a period for which amplitude is greater than half of the maximum amplitude
226 (Figure 6b) and has been used to represent the event duration of LFTs (e.g., Ide, 2010; Yabe
227 et al., 2019). We used simulated RMS envelopes at both DONET and virtual seismic stations
228 for detailed evaluation of spatial variations in amplitude and duration. The simulated
229 amplitude distribution did not show a simple two-lobe pattern, which is expected from the
230 assumed source mechanism. Generally, high-frequency maximum amplitude distribution is
231 distorted from the expected source radiation pattern by seismic wave scattering and
232 diffraction due to small-scale subsurface heterogeneities (e.g., Imperatori & Mai 2013;
233 Morioka et al. 2017; Takemura et al. 2009, 2016). Because we did not introduce small-scale
234 velocity heterogeneity into the reference model in this simulation, we confirmed that the
235 shallower heterogeneities, such as seawater and the thick low-velocity accretionary prism,
236 also distorted the maximum amplitude distribution. Thus, the assumption of isotropic
237 radiation for energy estimations of small offshore seismic events in many studies could be
238 suitable (e.g., Tamaribuchi et al., 2019; Yabe et al., 2019). Because our simulations did not
239 include site amplifications caused by structures with $V_S < 0.5$ km/s, the observed maximum
240 amplitude distribution could be more complicated due to site amplification factors at DONET
241 stations for high-frequency seismic waves (e.g., Kubo et al., 2018; Yabe et al., 2019).

242 Figures 6c and 6d show spatial variations and distance-change properties of half-duration
243 widths from the simulation result for a shallow LFT source. We also plotted the theoretical

244 values of t_q via the method of Sato & Emoto (2018) as a typical envelope broadening for
245 onshore earthquakes. Parameter t_q is defined as the time between S -wave onset and the time
246 when the RMS envelope decays to half the maximum amplitude. Although the half-value
247 widths exhibited heterogeneous distribution and were widely scattered, these values increased
248 with increasing distance and were of much longer duration than values of t_q (red lines). These
249 longer and distance-dependent S -wave durations could be caused by shallower heterogeneous
250 structures, such as seawater and the accretionary prism. Thus, to reliably estimate source
251 duration, the effects of elongation due to shallower structures should be incorporated.

252 On the other hand, the half-value widths for a simulated interplate earthquake did not
253 show distance-dependent properties (Figure 7). Some stations showed distinct reflection
254 phases from the sea surface or bedrock (Figures 4b, 5b, and 7b). Similar features appeared in
255 cases of an intraslab earthquake (Figure S4). These multiple reflections could cause step-like
256 elongation of half-value widths. Source durations of interplate earthquakes could be
257 overestimated if such multiple reflections are counted as the durations of S waves.
258 Conversely, by excluding such reflection phases and site amplifications from the analysis, the
259 source parameters of offshore regular earthquakes, which occurred at sufficient depths below
260 the accretionary prism, could be robustly estimated.

261 **4. Effects of heterogeneous structures on source parameter estimation for small seismic** 262 **events**

263 **4.1. Effects of heterogeneous structures on offshore seismograms**

264 We demonstrated that high-frequency seismic waves show complicated propagation in
265 offshore regions due to the influence of 3D heterogeneous structures. Our model in previous
266 3D simulations contains seawater, low-velocity accretionary prism, crust, and the subducting
267 Philippine Sea plate. According to the snapshots of simulated wavefield and differences in
268 simulated envelopes due to source locations, shallower heterogeneities could strongly affect
269 high-frequency seismic wave propagation. Shallower heterogeneities affect the maximum
270 amplitude distribution and envelope broadening of high-frequency seismic waves. At
271 frequencies greater than 1 Hz, characteristics of seismic wave propagation were usually
272 affected not only by deterministic layered structures but also small-scale velocity
273 heterogeneities along the propagation path (summarized in Ch. 2 of Sato et al., 2012). In this
274 sub-section, we discuss the effects of small-scale velocity heterogeneity, seawater, and low-
275 velocity accretionary prism on high-frequency seismic wave propagation through offshore
276 regions.

277 Small-scale velocity heterogeneities were modelled using stochastic random velocity
278 fluctuations characterized by an exponential autocorrelation function (ACF). The parameters
279 of small-scale velocity heterogeneity (correlation length and RMS value) within the slab
280 mantle and others were derived from Furumura & Kennett (2005) and Takemura et al. (2017),
281 respectively (see Table 3). We assumed the small-scale velocity heterogeneity within the
282 accretionary prism as same as that within the crust. Similar small-scale heterogeneity models
283 were previously used for waveform modelling in the Kanto sedimentary basin (Takemura &
284 Yoshimoto 2014).

285 We employ four heterogeneous models to discuss the effects of each heterogeneity on
286 offshore seismograms: model with small-scale velocity heterogeneity; model without a
287 seawater layer; model without an accretionary prism; and model without a seawater layer and
288 accretionary prism. The model with small-scale velocity heterogeneity was constructed by
289 superposing small-scale velocity heterogeneities (in Table 3) on the reference model. In the
290 model without the seawater layer, the physical parameters within the seawater layer were
291 replaced with those within the air column, and the seafloor was treated as the free surface. In
292 the model without the low-velocity accretionary prism, physical parameters were replaced
293 with those of the upper crust (Table 1). All models included bathymetry, but we do not
294 discuss its effects because previous studies have reported limited effects of topographic
295 scattering on body wave propagation (e.g., Imperatori & Mai, 2015; Takemura et al., 2015).

296 Figure 8 shows the simulated RMS envelopes at DONET stations using the four different
297 heterogeneous models. To visualize the effects of heterogeneities, RMS envelopes of the
298 reference model were also plotted by grey lines. Although maximum amplitudes and later
299 phases were slightly changed by introducing small-scale velocity heterogeneities, these
300 effects were not significant (Figure 8a). This tendency remains unchanged when using
301 stronger models or those with different random seeds (Figure S5). In typical crustal
302 earthquakes, the effects of small-scale velocity heterogeneity appear as amplitude fluctuations
303 of high-frequency seismic waves even for stations at shorter distances (e.g., Yoshimoto et al.,
304 2015). Numerical simulations by Iwaki et al. (2018) showed that crustal small-scale
305 heterogeneity has limited effects on ground motions for frequencies lower than 1 Hz in the
306 Kanto sedimentary basin. Our large-scale simulations demonstrate that the effects of the
307 sedimentary layers (accretionary prism) on high-frequency seismic waves are stronger than
308 those of small-scale velocity heterogeneity.

309 In the model without seawater, the seafloor was treated as the free surface and,

310 consequently, RMS amplitudes were amplified (Figure 8b). The low-velocity accretionary
311 prism has dominant effects on high-frequency seismic waves in this region. The model
312 without the accretionary prism exhibited simple pulse-like RMS envelopes, which are very
313 similar to the typical envelopes of onshore small earthquakes (Figure 8c). Pulse-like *S* waves
314 and multiple small pulses after *S* waves were found in simulated RMS envelopes. The
315 differences between the RMS envelopes of the reference model and the model without the
316 accretionary prism indicate that elongations of *S* waves at offshore stations were mostly
317 caused by the low-velocity accretionary prism.

318 Multiple later packets after *S* waves are weak but also present in the RMS envelopes of the
319 model without both seawater and accretionary prism (Figure 8d). These phases could be
320 interpreted as reflections from the subducting Philippine Sea slab. It is difficult to find the
321 phases reflected from the subducting Philippine Sea slab in the RMS envelopes of the model
322 that includes the accretionary prism, as the elongation and amplification effects of the
323 accretionary prism masked reflections from the Philippine Sea plate. Tonegawa et al. (2015)
324 also reported that reflections from the bedrock (bottom of oceanic sediments) are also
325 dominant in ambient noise wavefields, and it is difficult to identify reflections from the
326 boundaries at depths below the bedrock.

327 According to the above results, we conclude that the low-velocity accretionary prism is
328 dominant influence on high-frequency seismic wave propagation through the offshore region,
329 whereas other heterogeneities, such as seawater and small-scale velocity heterogeneities,
330 have minor effects. Similar tendencies were also found in simulations of interplate and
331 intraslab earthquakes (Figures S6 and S7). The low-velocity accretionary prism is also
332 important for low-frequency surface wave propagation (e.g., Takemura, Kubo, et al. 2019;
333 Volk et al. 2017). Strong amplification or waveguide effects for both low- and high-frequency
334 seismic waves due to the accretionary prism were also reported in the Cascadia, Mexico, and
335 Hikurangi subduction zones (e.g., Gomberg, 2018; Kaneko et al., 2019; Shapiro et al., 2000).
336 To achieve reliable modelling of broadband seismic wave propagation through offshore
337 regions, and precise source-parameter estimations for offshore seismic events, a detailed
338 model of the low-velocity accretionary prism should be considered.

339 **4.2. Source parameter estimation for a shallow LFT via the conventional method**

340 For small events, especially LFTs, the durations, source energies or band-limited moments
341 have been estimated by using stacked coherent RMS envelopes or average values for the used
342 stations after correction of site amplification and attenuations (e.g., Annoura et al., 2016;

343 Ghosh et al., 2009; Kao et al., 2010; Maeda & Obara, 2009; Yabe et al., 2019; Yabe & Ide,
344 2014). However, our simulations demonstrated that elongation of RMS envelopes for a
345 shallow LFT, due to the low-velocity accretionary prism, occur even for stations as close as
346 10 km from the epicentre (Figures 4a and 6). Thus, incorrect estimation of source parameters
347 via the conventional method could be expected. In this sub-section we conducted an FDM
348 simulation of seismic wave propagation and compared it with observed RMS envelopes to
349 investigate the validity and limitations of STF's estimation by the conventional method.

350 We used observed DONET seismograms for a shallow LFT that occurred at 11:18 on 24
351 October 2015 (JST), located at 136.91°E, 33.35°N. For deep slow earthquakes, the
352 proportionality between seismic energy rate functions estimated from high-frequency
353 seismograms and seismic moment rate functions estimated from low-frequency seismograms
354 is confirmed (Ide et al., 2008). Yabe et al. (2019) showed that the same proportionality holds
355 true for shallow slow earthquakes. Therefore, seismic energy rate functions estimated from
356 high-frequency seismograms can be converted into STF's by dividing them by the value of
357 scaled energy. The seismic energy rate function of the event observed at each station is
358 conventionally calculated from squared seismograms at each station after correction of site
359 and attenuation effects within time windows of half-value width measured for stacked RMS
360 envelope. Seismograms were excluded from the analysis if the cross-correlation coefficient
361 with the same event envelopes at any other stations did not exceed 0.6. This procedure
362 removed stations lacking tremor signals. Modelling for direct-*S* wave energies using the
363 uniform background velocity structure ($V_s = 3.5$ km/s and $\rho = 2700$ kg/m³) and distance-
364 dependent attenuation model (Figure 3 of Yabe et al., 2019) was employed. The seismic
365 energy rate functions are converted into STF's, assuming a scaled energy value of 3.0×10^{-9}
366 (Ide & Maury, 2018; Ide & Yabe, 2014; Yabe et al., 2019). The STF of the event is calculated
367 by stacking STF's at each station after applying a 10 s low-pass filter.

368 Figure 9 shows the STF's of a shallow LFT that occurred on 24 October 2015. The
369 conventional method typically provided STF's represented by blue dashed or red lines, which
370 were estimated by using stacking seismic energy rate functions of B-node stations and B- and
371 C-node stations, respectively. The moment releases of these STF's continued 50–60 s from the
372 origin and peaks of moment rate appeared at around 25 s. The STF described by the solid-
373 blue line was constructed by using the seismic energy rate function at M.KMB06 only, which
374 was located just above the shallow LFT hypocentre. This STF was completely different from
375 the others. The peak of this STF appeared within 3.2 s of the origin, and moment release

376 continued 30–40 s from the origin. By using these STFs, we synthesized seismograms of the
377 shallow LFT. Hypocentre depth was fixed on the plate boundary and the focal mechanism
378 was the same as in previous simulations of event A (Table 2). During an FDM simulation of
379 seismic wave propagation, we assumed a simple 0.1 s triangle function, which was enough
380 shorter than STFs in Figure 9. After FDM simulations, we convolved the estimated STFs to
381 simulated envelopes.

382 Figure 10 compares 1–5 Hz RMS envelopes between simulations and observations. In this
383 comparison the amplitudes of each trace were normalized by each maximum amplitude
384 because precise seismic moment and site amplification factors from the $V_S = 0.5$ km/s layer
385 were not well known. The analysis focused on differences in envelope shapes between
386 simulations and observations. The simulation results with the STF from M.KMB06
387 reproduced the observed envelope shapes and durations at all stations. This STF also
388 reproduced the seismograms observed for a shallow VLFE (Yabe et al., 2019), which
389 occurred in the same time window as the target shallow LFT but appeared for frequencies of
390 0.03–0.05 Hz. The simulations with the other STFs were much longer than the observations.
391 Two of the simulated STFs also showed delayed peak amplitudes compared to the
392 observations. The epicentral distances of B-node stations except for M.KMB06 range from
393 10 to 16 km. The simulation with a simple STF (Figure 4a and Figure 6) demonstrated that
394 the durations of S waves increased rapidly with increasing distance, and reached to 5–15 s at
395 stations located at distances of 10–15 km. Thus, STFs from stacked seismic energy rate
396 functions via the conventional method were delayed and overestimated. The simulation with
397 a simple STF of duration 0.2 s (see Figure 4a) shows that the RMS envelopes at very close
398 (< 10 km) stations are characterized by a pulse-like S wave packet, and consequently, seismic
399 energy rate functions at close stations could preserve source information. Thus, the shapes
400 and durations of observed RMS envelopes were only well reproduced in the STF estimated
401 from the nearest station (~ 1.4 km, M.KMB06).

402 Our numerical tests in this sub-section revealed that STFs from stations very close to the
403 source reproduced the observed seismogram envelopes of the target shallow LFT. In other
404 words, the effects of offshore heterogeneities are limited at stations with epicentral distances
405 less than 10 km, and, consequently, the source parameter information is preserved. At stations
406 with epicentral distances greater than approximately 10 km, RMS envelopes were strongly
407 elongated due to the effects of the accretionary prism (Figure 4a). At stations with epicentral
408 distances greater than approximately 10 km, durations of the RMS envelope were controlled

409 by the heterogeneous structure of the accretionary prism along the propagation path. Thus,
410 STFs calculated using such stations via the conventional method (e.g., Yabe et al., 2019) were
411 overestimated and could not reproduce the observed RMS envelopes. When the conventional
412 method is applied to OBS data, seismograms should be selected from stations located closer
413 than approximately 10 km. If stations further than 10 km from the source are used, the effects
414 of 3D offshore heterogeneities should be included in the method of source parameter
415 estimation.

416 **5. Conclusions**

417 We investigated the effects of offshore heterogeneities, such as small-scale velocity
418 heterogeneity, seawater, and accretionary prism, on high-frequency seismic propagation
419 southeast off the Kii Peninsula, southwest Japan. Our simulations demonstrated that the low-
420 velocity accretionary prism affects the shapes of seismogram envelopes. A thick low-velocity
421 accretionary prism is also developed in the Cascadia, Mexico, and Hikurangi subduction
422 zones, and affects not only low-frequency surface waves but also high-frequency seismic
423 waves. The effects of the accretionary prism are significant in cases of shallow LFT sources,
424 as these sources are typically located just beneath the accretionary prism toe at depths of 5–8
425 km near the trench axis. On the other hand, because interplate and intraslab earthquakes in
426 this region occur at sufficient depths below the low-velocity accretionary prism, seismogram
427 envelopes comprise multiple pulse-like wave packets that consist of direct-*S* waves and
428 multiple reflections from the bedrock.

429 The seismogram envelopes of a source at shallow LFT depths are broadened due to the
430 low-velocity accretionary prism, even when assuming a simple STF. The durations of RMS
431 envelopes exceed 10 s, even at stations located at distances greater than 10 km. Multiple
432 reflected phases found in seismograms of regular earthquakes also affect half-value widths.
433 Such elongation of envelopes causes incorrect estimation of event durations. Event durations
434 are important for discussing the scaling law of regular and slow earthquakes. After removing
435 such reflection phases and site amplification from the analysis, the source parameters of
436 offshore regular earthquakes, which occurred at sufficient depths below the accretionary
437 prism, could be reliably estimated.

438 At stations very close (< 10 km) to the source, pulse-like *S* wave envelopes, reflecting an
439 assumed STF, are preserved. If stations at distances greater than 10 km are used, STF could
440 be overestimated in terms of duration and peak time of the moment rate. By estimating STF
441 using only the nearest stations, the FDM simulation reproduced the shapes and durations of

442 observed RMS envelopes. By incorporating site amplification due to lower velocity
443 sediments ($V_s < 0.5$ km/s) at each station, the Green's functions of numerical simulations in a
444 3D local model potentially enables reliable source parameter estimations for small offshore
445 events in future studies.

446 **Acknowledgements**

447 F-net and DONET waveform data are available via the NIED website
448 (<https://doi.org/10.17598/NIED.0005>, <https://doi.org/10.17598/NIED.0008>). Bathymetric
449 depth data were obtained from ETOPO1 (Amante & Eakins, 2009). OpenSWPC software
450 (Maeda et al., 2017) and the 3D model of Koketsu et al. (2012) were obtained from
451 <https://doi.org/10.5281/zenodo.3712650> and
452 https://www.jishin.go.jp/evaluation/seismic_hazard_map/lpshm/12_choshuki_dat/,
453 respectively. Generic Mapping Tools (GMT; Wessel et al., 2013) and Seismic Analysis Code
454 (SAC; Helffrich *et al.* 2013) were used to produce the figures and in signal processing,
455 respectively. The catalogues of slow earthquakes (Nakano, Hori, *et al.* 2018, Takemura *et al.*
456 2019) were downloaded from the Slow Earthquake Database website (Kano et al., 2018;
457 <http://www-solid.eps.s.u-tokyo.ac.jp/~sloweq/>). The CMT results of the 2016 southeast off
458 Kii Peninsula earthquake, Japan, and an intraslab earthquake, used in regular earthquake
459 simulations, are available from <https://doi.org/10.5281/zenodo.3523583>. We also used the
460 unified hypocentre catalogue of the Japan Meteorological Agency
461 (<https://www.data.jma.go.jp/svd/eqev/data/bulletin/index.html>). The FDM simulations of
462 seismic wave propagation were conducted using the Earth Simulator of JAMSTEC. This
463 study was supported by the Japan Society for the Promotion of Science (JSPS) KAKENHI
464 Grant Numbers 17K14382, 18K13639 in Grant-in-aid for Young Scientists and 19H04626 in
465 Scientific Research under Innovative Areas 'Science of Slow Earthquakes'.

466

467 **Tables**

468 **Table 1.** Physical parameters of each layer of the 3D velocity structure model. The
 469 parameters were obtained from the Japan Integrated Velocity Structure Model (JIVSM)
 470 (Koketsu et al., 2012). The air and seawater layers were treated as being the same,
 471 following Maeda *et al.* (2017).

	V_P [km/s]	V_S [km/s]	ρ [kg/m ³]	Q_P	Q_S
Air	0.0	0.0	0.001	10^{10}	10^{10}
seawater	1.5	0.0	1.04	10^6	10^6
Sedimentary layer 1	1.8	0.5	1.95	170	100
Sedimentary layer 2	2.2	0.8	2.07	272	160
Sedimentary layer 3	2.4	1.0	2.15	340	200
Sedimentary layer 4	3.0	1.5	2.25	510	300
Sedimentary layer 5	3.5	2.0	2.35	680	400
Basement	5.5	3.2	2.65	680	400
Upper crust	5.8	3.4	2.70	680	400
Lower crust	6.4	3.8	2.80	680	400
Upper mantle	7.5	4.5	3.20	850	500
Philippine Sea plate					
Oceanic crust layer 2	5.0	2.9	2.40	340	200
Oceanic crust layer 3	6.8	4.0	2.90	510	300
Oceanic Mantle	8.0	4.7	3.20	850	500

472

473

474 **Table 2.** Source parameters used in FDM simulations. A shallow LFT and intraslab
 475 earthquakes were referred from the nearest shallow VLFE and intraslab earthquakes of
 476 CMT solutions in our previous studies (Takemura, Okuwaki, *et al.* 2019, Takemura *et al.*
 477 2019). Double-couple point sources were assumed. The value of T_0 represents the STF
 478 duration.

	Type	Lon. [E°]	Lat. [°N]	Depth [km]	Strike [°]	Dip [°]	Rake [°]	M_w	T_0 [s]
A	LFT	136.90	33.20	6.20	255.0	7.0	116.0	3	0.2
B	Interplate earthquake	136.34	33.40	11.15	243.3	10.1	114.4	3	0.2
C	Intraslab earthquake	137.11	33.28	28.7	264.3	37.9	37.9	3	0.2

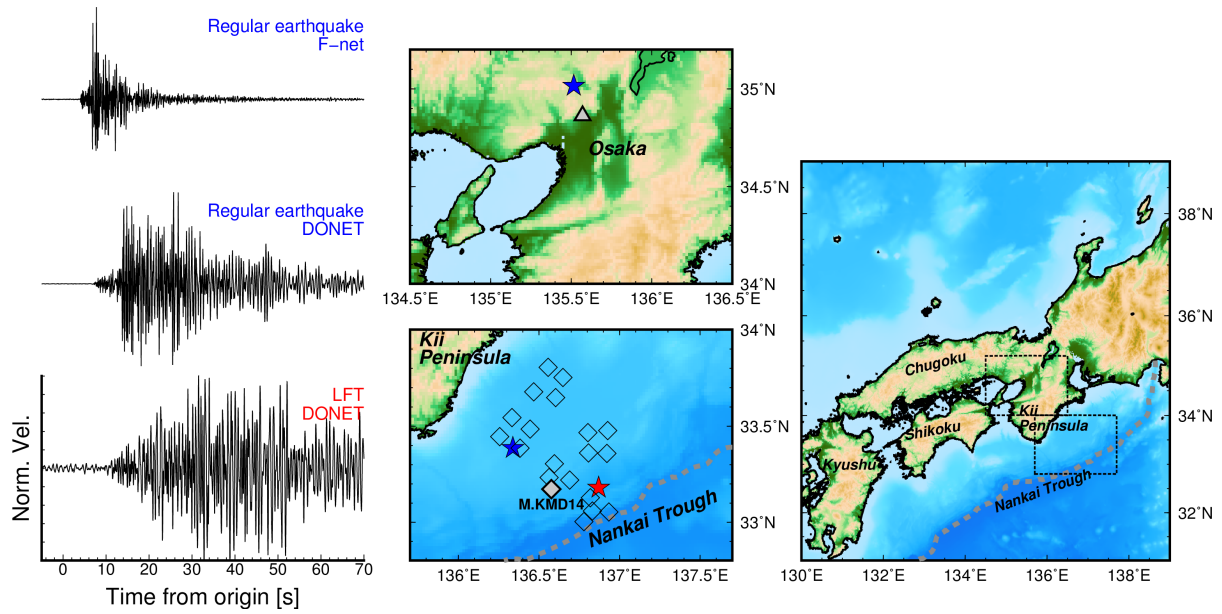
479
 480 **Table 3.** Parameters of small-scale velocity heterogeneities in each layer. The models of the
 481 crust and oceanic crust were assumed to be the same as the model of crustal
 482 heterogeneity (Takemura *et al.* 2017). The model of the oceanic mantle derives from
 483 Furumura & Kennett (2005).

Layer	ACF-type	Correlation length a	RMS value ε
Air and seawater	-	-	-
Accretionary prism	Exponential	Isotropic 1 km	0.03
Crust	Exponential	Isotropic 1 km	0.03
Mantle	-	-	-
Oceanic crust	Exponential	Isotropic 1 km	0.03
Oceanic mantle	Exponential	Horizontal: 10 km Vertical: 0.5 km	0.03

484

485

486 **Figures**

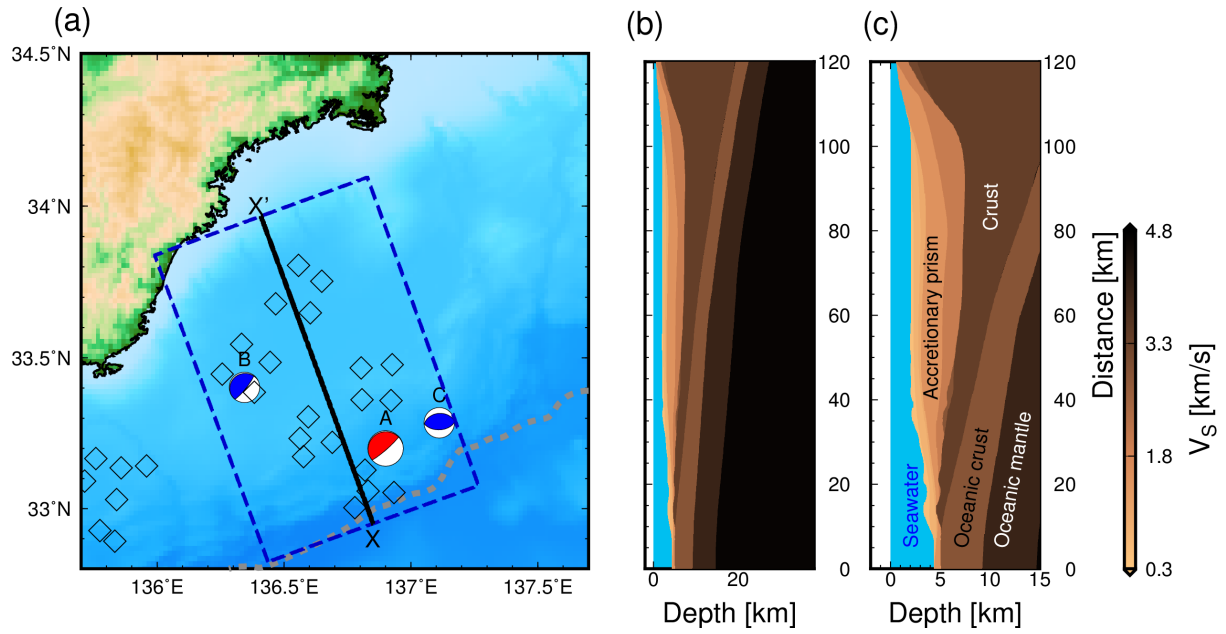


487

488 **Figure 1.** Examples of observed NS-component seismograms for a crustal earthquake, an
 489 offshore interplate earthquake and a shallow LFT. Crustal and offshore interplate
 490 earthquakes occurred on 24 January 2015 and 1 April 2016, respectively. A shallow LFT
 491 occurred on 3 April 2016. The magnitudes of these events are approximately 3, and
 492 epicentral distances are also similar. The blue stars and red star in enlarged maps are the
 493 epicentres of regular earthquakes and shallow LFT, respectively. The triangle and
 494 diamond symbols locate the F-net and DONET stations, respectively.

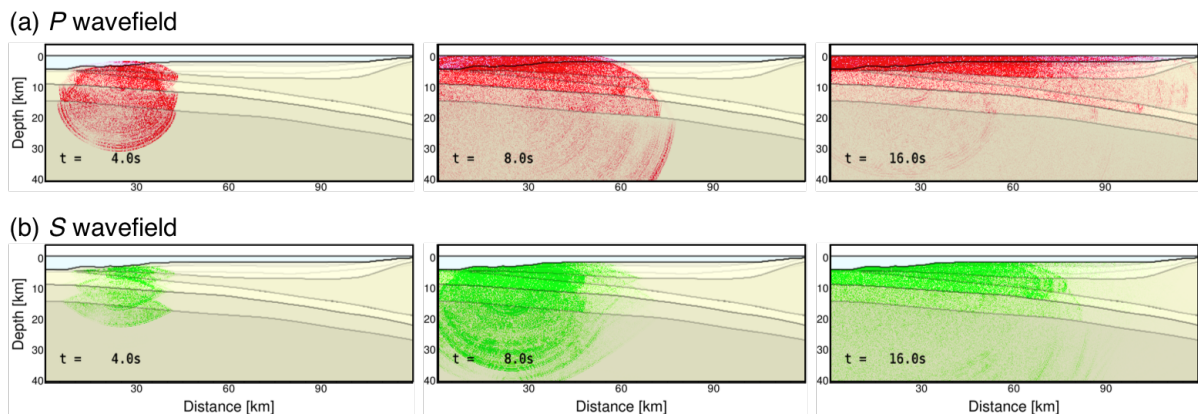
495

496



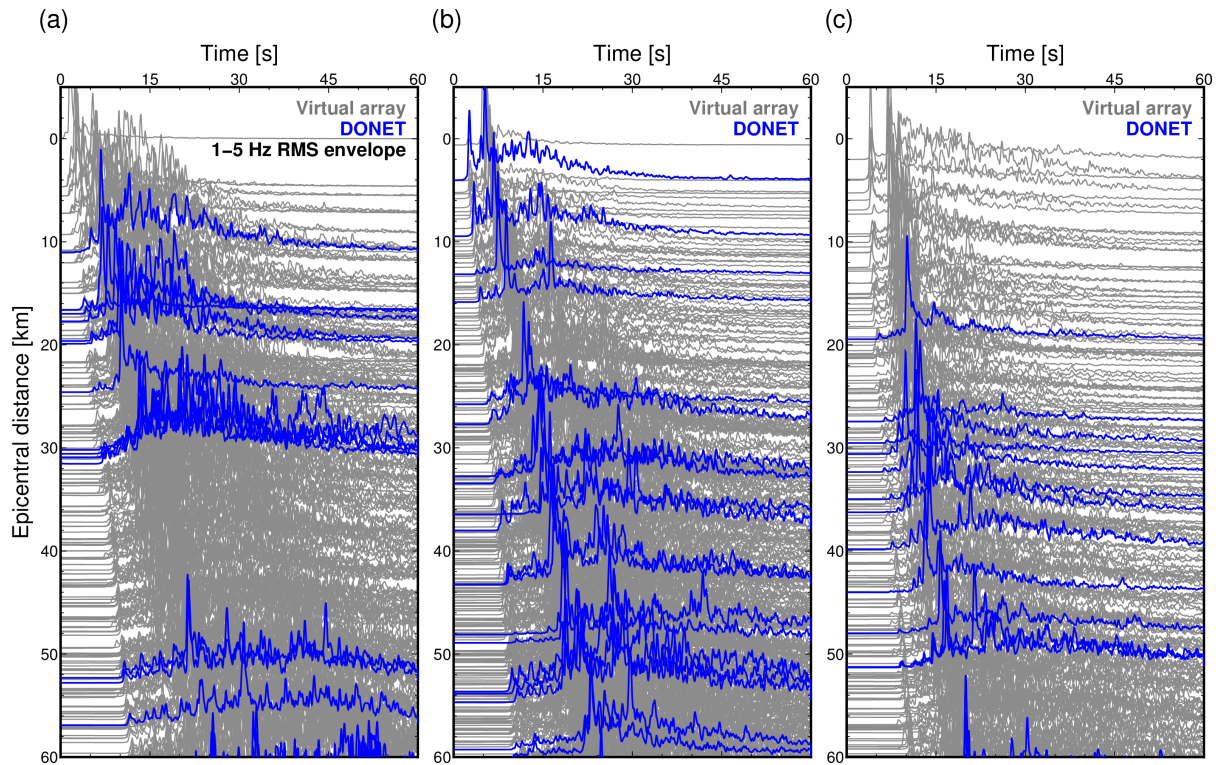
497
498
499
500
501
502

Figure 2. (a) Map of the simulation region, cross-sections of (b) S -wave velocity model along X—X' profile and (c) S -wave velocity model at shallower (<15 km) depths. The red and blue focal mechanisms are source models of a shallow LFT and regular earthquakes, respectively. Details of physical parameters in each layer are listed in Table 1.



503
504
505
506

Figure 3. Simulated snapshots of: (a) P , and (b) S wavefields along profile X—X' for the shallow LFT simulation (red focal sphere in Figure 2).



507

508

509

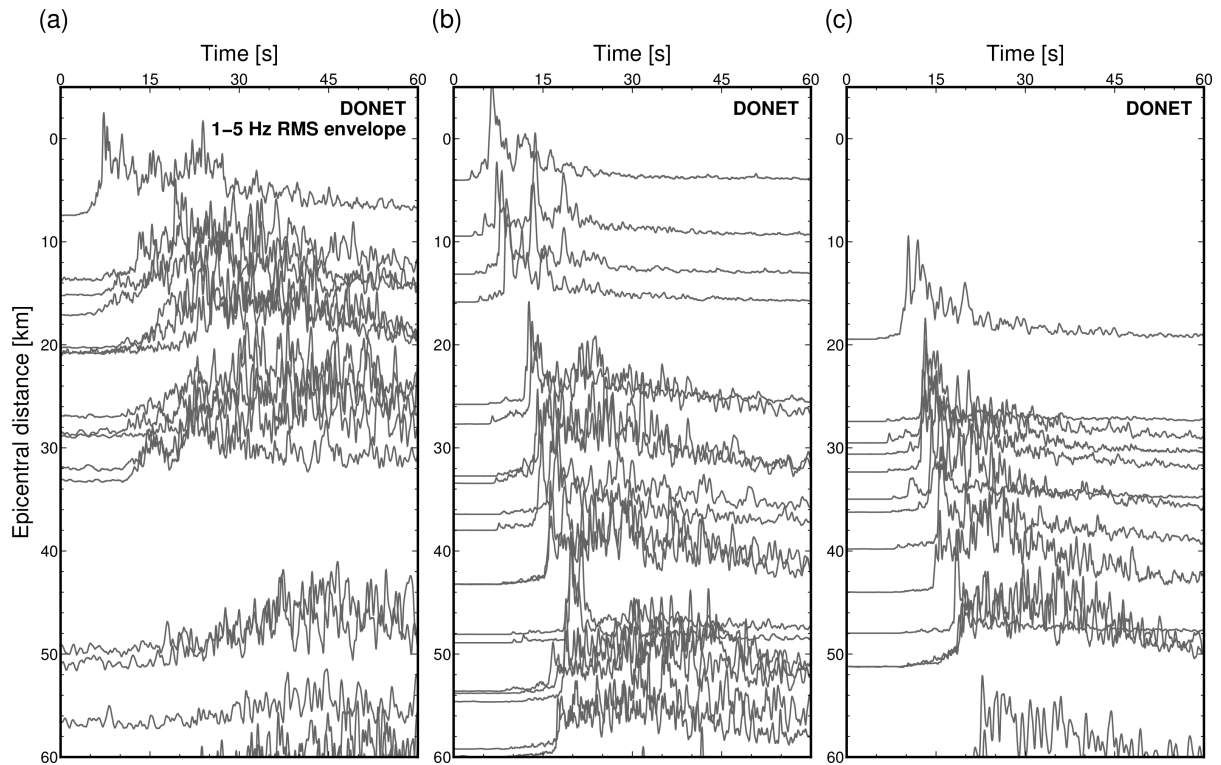
510

511

512

513

Figure 4. Simulated RMS envelopes for frequencies of 1–5 Hz from simulations of: (a) shallow LFT, (b) interplate earthquake and (c) intraslab earthquake. Source parameters and locations are shown in Table 2 and Figure 2a. RMS envelopes at DONET and virtual stations are represented by blue and grey lines, respectively.



514

515

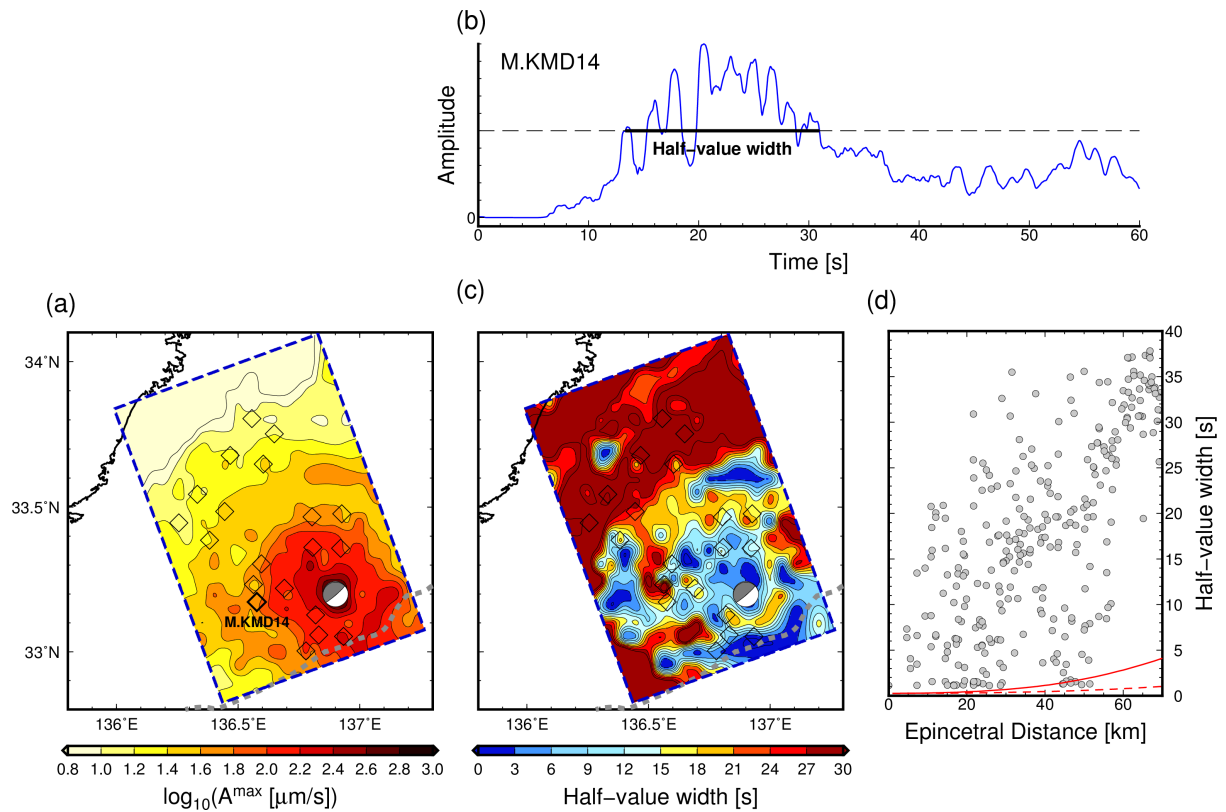
516

517

518

519

Figure 5. Observed RMS envelopes for frequencies of 1–5 Hz at DONET stations. RMS envelopes for: (a) a shallow LFT on 16 April 2016, (b) an interplate earthquake on 19 April 2016 and (c) an intraplate earthquake on 4 December 2014.



520

521 **Figure 6.** Spatial variations of maximum RMS amplitudes and half-value widths of simulated

522 RMS envelopes for a shallow LFT: (a) Maximum RMS amplitude distribution, (b) an

523 example of half-value width estimations, (c) half-value width distribution and (d) half-

524 value widths as a function of epicentral distance. An example in (b) is an RMS envelope

525 at M.MRD14 (location shown in (a)). The red dashed and solid lines in (d) are values of

526 t_q via the method of Sato & Emoto (2018). Here, t_q is defined as the time between *S*-

527 wave onset and the time when the RMS envelope decays to half the maximum

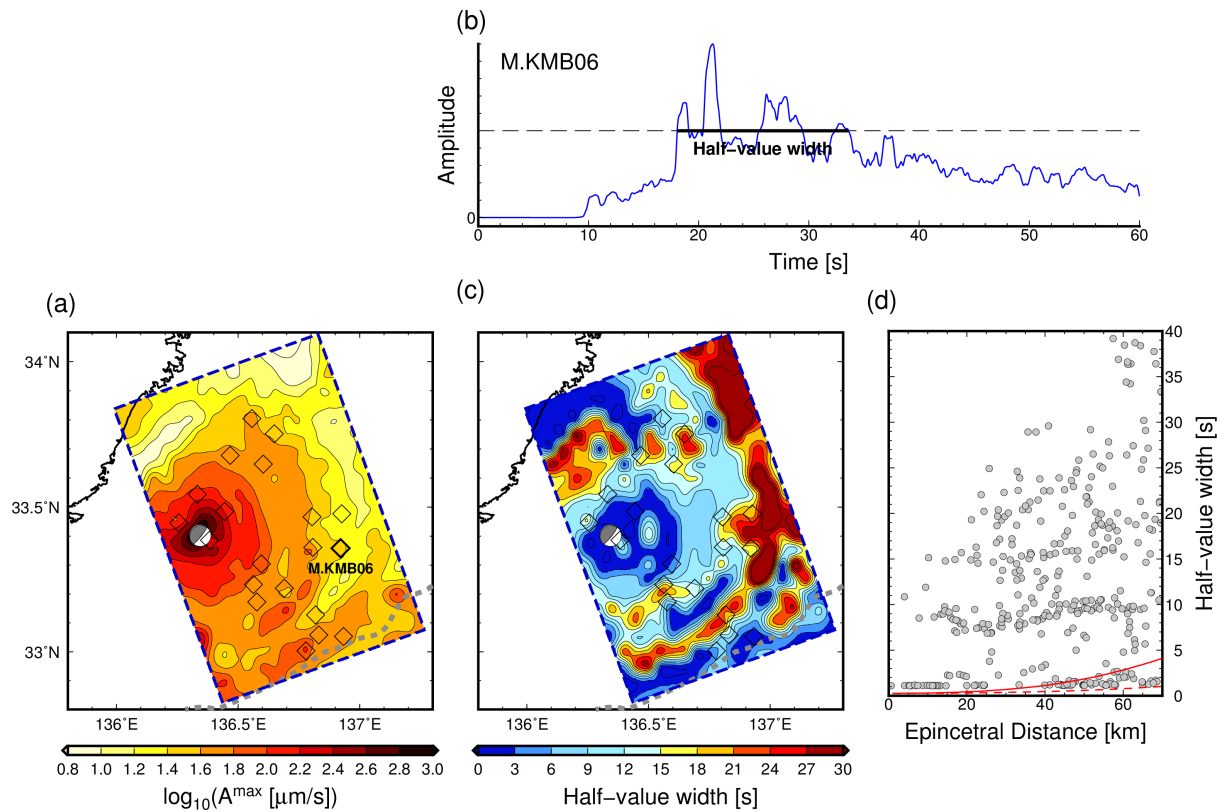
528 amplitude. The assumed small-scale random velocity heterogeneity models for dashed

529 and solid lines are characterized by an exponential-type autocorrelation function with

530 correlation length of 1 km and RMS values of 0.03 and 0.05, respectively. The central

531 frequency in theoretical synthetics is 4 Hz.

532



533

534 **Figure 7.** Spatial variations of maximum RMS amplitudes and half-value widths of simulated

535 RMS envelopes for an interplate earthquake: (a) Maximum RMS amplitude distribution,

536 (b) an example of half-value width estimations, (c) half-value width distribution and (d)

537 half-value widths as a function of epicentral distance. An example in (b) is an RMS

538 envelope at M.MRB06 (location shown in (a)). The red dashed and solid lines in (d) are

539 values of t_q via the method of Sato & Emoto (2018). Here, t_q is defined as the time

540 between S -wave onset and the time when the RMS envelope decays to half the maximum

541 amplitude. The assumed small-scale random velocity heterogeneity models for dashed

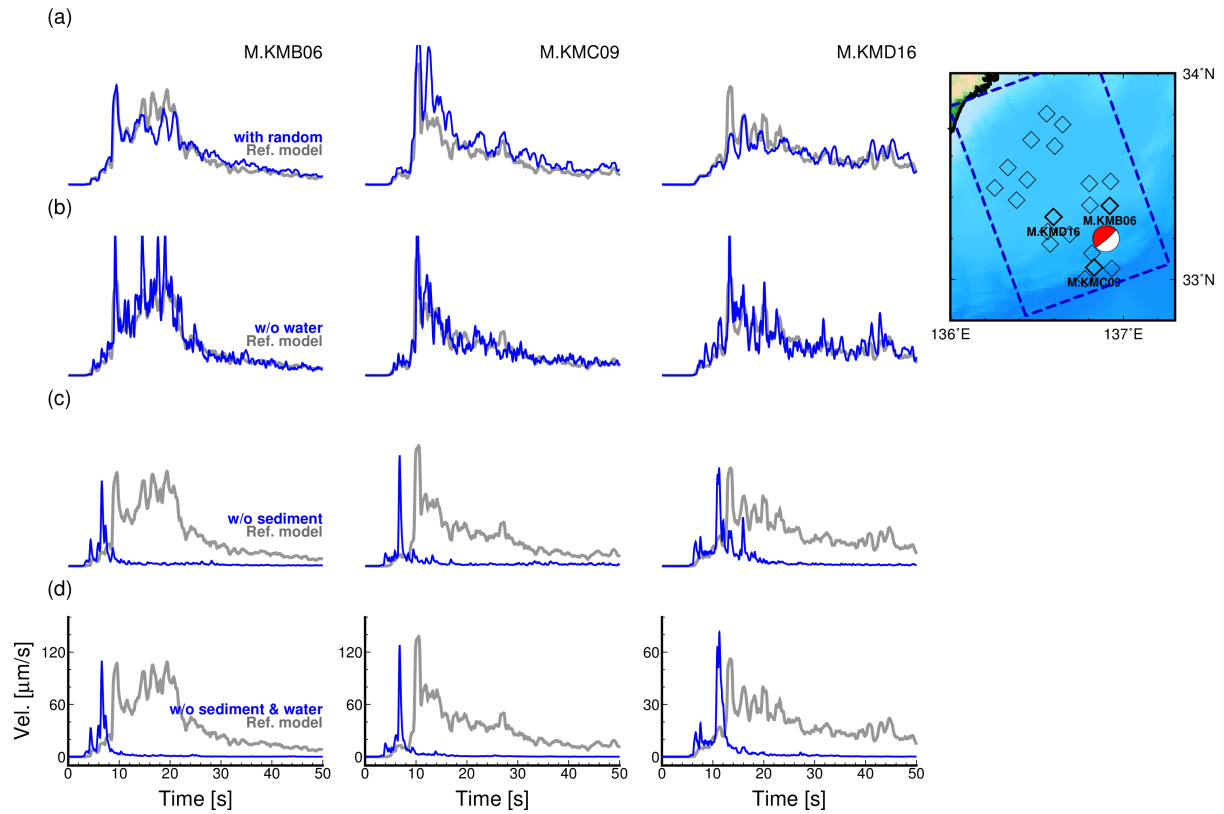
542 and solid lines are characterized by an exponential-type autocorrelation function with

543 correlation length of 1 km and RMS values of 0.03 and 0.05, respectively. The central

544 frequency in theoretical synthetics is 4 Hz.

545

546



547

548

549

550

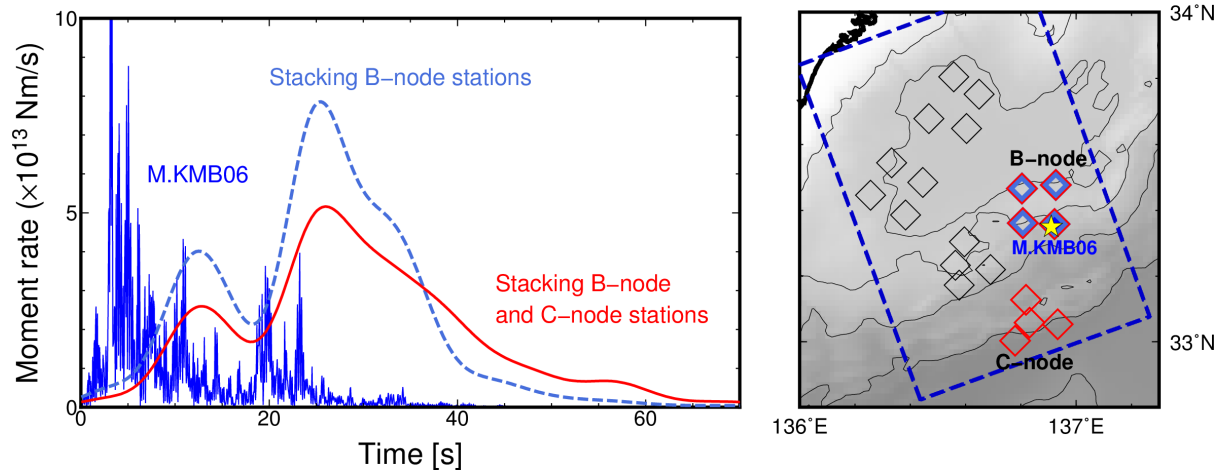
551

552

553

554

Figure 8. Simulation results of various heterogeneous models for a shallow LFT. The blue lines are RMS envelopes derived from models: (a) with small-scale random velocity heterogeneities, (b) without seawater, (c) without oceanic sediments (accretionary prism) and (d) without oceanic sediments and seawater. Grey lines are the simulation results with the reference model.



555

556

557

558

559

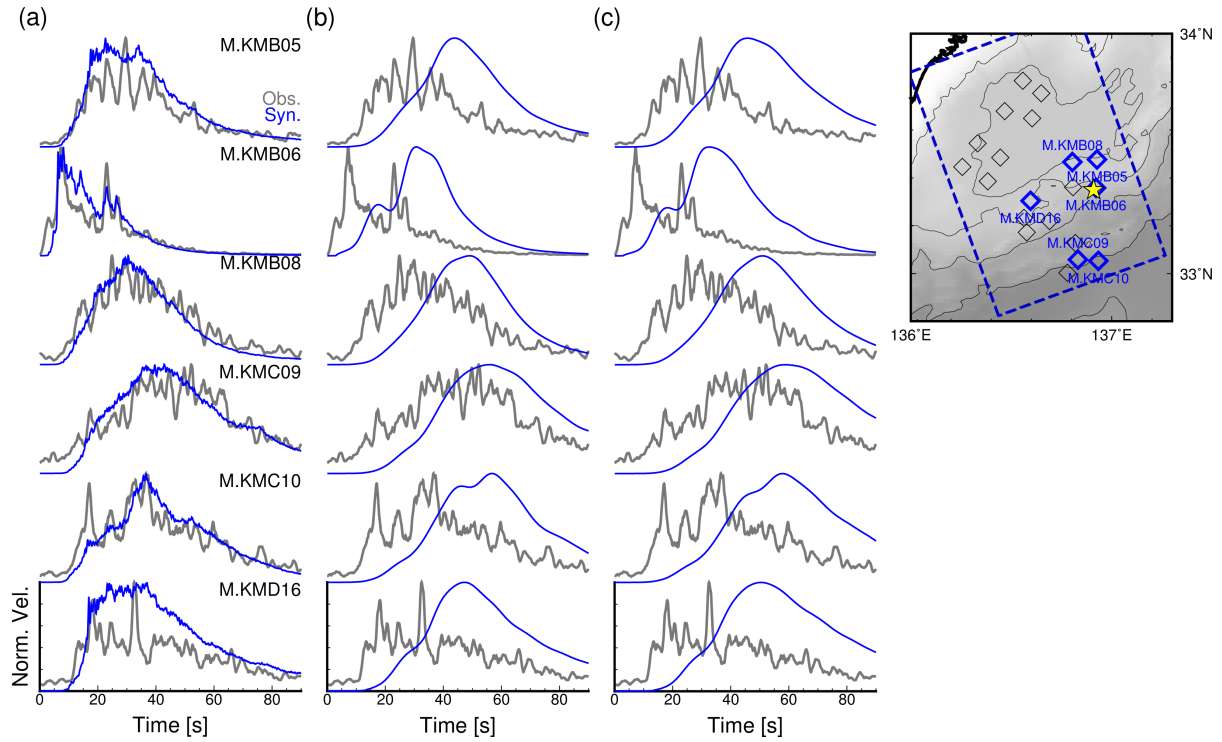
560

561

562

563

Figure 9. Source time functions (STFs) estimated from observed RMS envelopes of a shallow LFT at 11:18 on 24 October 2015 (JST). The blue dashed blue and red lines are source time functions estimated from the RMS envelope of M.KMB06, envelopes of B-node stations and envelopes of B- and C-node stations, respectively. The yellow star on the map is the epicentre. The epicentral distance of M.KMB06 is 1.4 km. The stations represented by coloured symbols are used in the STF estimation for correspondingly coloured lines.



564

565

Figure 10. Comparison between simulated RMS envelopes with observations. RMS

566

envelopes were synthesized from simulation results of source time functions estimated

567

using: (a) M.KMB06, (b) B-node stations and (c) B- and C-node stations. Because

568

precise seismic moment for a target shallow LFT and site amplification factors were not

569

well known, the amplitudes of each trace were normalized by each maximum amplitude.

570

The upper-right panel shows the stations used (blue diamonds) and the epicentre location

571

(yellow star).

572

573

574 **References**

- 575 Amante, C., & Eakins, B. W. (2009). ETOPO1 1 arc-minute global relief model: Procedures,
576 data sources and analysis. NOAA Technical Memorandum NESDIS NGDC-24. *NOAA*
577 *Technical Memorandum NESDIS NGDC-24. National Geophysical Data Center, NOAA,*
578 (March), 19. <https://doi.org/10.7289/V5C8276M>
- 579 Ando, M. (1975). Source mechanisms and tectonic significance of historical earthquakes
580 along the Nankai trough, Japan. *Tectonophysics*, 27(2), 119–140.
581 [https://doi.org/10.1016/0040-1951\(75\)90102-X](https://doi.org/10.1016/0040-1951(75)90102-X)
- 582 Annoura, S., Obara, K., & Maeda, T. (2016). Total energy of deep low-frequency tremor in
583 the Nankai subduction zone, southwest Japan. *Geophysical Research Letters*, 43(6),
584 2562–2567. <https://doi.org/10.1002/2016GL067780>
- 585 Annoura, S., Hashimoto, T., Kamaya, N., & Katsumata, A. (2017). Shallow episodic tremor
586 near the Nankai Trough axis off southeast Mie prefecture, Japan. *Geophysical Research*
587 *Letters*, 44(8), 3564–3571. <https://doi.org/10.1002/2017GL073006>
- 588 Araki, E., Saffer, D. M., Kopf, A. J., Wallace, L. M., Kimura, T., Machida, Y., et al. (2017).
589 Recurring and triggered slow-slip events near the trench at the Nankai Trough
590 subduction megathrust. *Science*, 356(6343), 1157–1160.
591 <https://doi.org/10.1126/science.aan3120>
- 592 Battaglia, J., & Aki, K. (2003). Location of seismic events and eruptive fissures on the Piton
593 de la Fournaise volcano using seismic amplitudes. *Journal of Geophysical Research*,
594 108(B8), 2364. <https://doi.org/10.1029/2002JB002193>
- 595 Carcolé, E., & Sato, H. (2010). Spatial distribution of scattering loss and intrinsic absorption
596 of short-period S waves in the lithosphere of Japan on the basis of the Multiple Lapse
597 Time Window Analysis of Hi-net data. *Geophysical Journal International*, 180(1), 268–
598 290. <https://doi.org/10.1111/j.1365-246X.2009.04394.x>
- 599 Chaput, J., Campillo, M., Aster, R. C., Roux, P., Kyle, P. R., Knox, H., & Czoski, P. (2015).
600 Multiple scattering from icequakes at Erebus volcano, Antarctica: Implications for
601 imaging at glaciated volcanoes. *Journal of Geophysical Research: Solid Earth*, 120(2),
602 1129–1141. <https://doi.org/10.1002/2014JB011278>
- 603 Ekström, G., Nettles, M., & Dziewoński, A. M. (2012). The global CMT project 2004-2010:
604 Centroid-moment tensors for 13,017 earthquakes. *Physics of the Earth and Planetary*
605 *Interiors*, 200–201, 1–9. <https://doi.org/10.1016/j.pepi.2012.04.002>
- 606 Ellsworth, W. L., & Bulut, F. (2018). Nucleation of the 1999 Izmit earthquake by a triggered
607 cascade of foreshocks. *Nature Geoscience*, 11(7), 531–535.
608 <https://doi.org/10.1038/s41561-018-0145-1>
- 609 Fletcher, J. B., & McGarr, A. (2011). Moments, magnitudes, and radiated energies of non-
610 volcanic tremor near Cholame, CA, from ground motion spectra at UPSAR.
611 *Geophysical Research Letters*, 38(16), n/a-n/a. <https://doi.org/10.1029/2011GL048636>

- 612 Furumura, T., & Kennett, B. L. N. (2005). Subduction zone guided waves and the
613 heterogeneity structure of the subducted plate: Intensity anomalies in northern Japan.
614 *Journal of Geophysical Research*, 110(B10), B10302.
615 <https://doi.org/10.1029/2004JB003486>
- 616 Furumura, Takashi, & Kennett, B. L. N. (2018). Regional Distance PL Phase in the Crustal
617 Waveguide-An Analog to the Teleseismic W Phase in the Upper-Mantle Waveguide.
618 *Journal of Geophysical Research: Solid Earth*, 123(5), 4007–4024.
619 <https://doi.org/10.1029/2018JB015717>
- 620 Ghosh, A., Vidale, J. E., Sweet, J. R., Creager, K. C., & Wech, A. G. (2009). Tremor patches
621 in Cascadia revealed by seismic array analysis. *Geophysical Research Letters*, 36(17),
622 L17316. <https://doi.org/10.1029/2009GL039080>
- 623 Gomberg, J. (2018). Cascadia Onshore-Offshore Site Response, Submarine Sediment
624 Mobilization, and Earthquake Recurrence. *Journal of Geophysical Research: Solid
625 Earth*, 123(2), 1381–1404. <https://doi.org/10.1002/2017JB014985>
- 626 Gomberg, J., Wech, A., Creager, K., Obara, K., & Agnew, D. (2016). Reconsidering
627 earthquake scaling. *Geophysical Research Letters*, 43(12), 6243–6251.
628 <https://doi.org/10.1002/2016GL069967>
- 629 Guo, Y., Koketsu, K., & Miyake, H. (2016). Propagation mechanism of long-period ground
630 motions for offshore earthquakes along the nankai trough: Effects of the accretionary
631 wedge. *Bulletin of the Seismological Society of America*, 106(3), 1176–1197.
632 <https://doi.org/10.1785/0120150315>
- 633 Gusev, A. A., & Pavlov, V. M. (1991). Deconvolution of squared velocity waveform as
634 applied to the study of a noncoherent short-period radiator in the earthquake source.
635 *Pure and Applied Geophysics*, 136(2–3), 235–244. <https://doi.org/10.1007/BF00876375>
- 636 Hawthorne, J. C., Thomas, A. M., & Ampuero, J.-P. (2019). The rupture extent of low
637 frequency earthquakes near Parkfield, CA. *Geophysical Journal International*, 216(1),
638 621–639. <https://doi.org/10.1093/gji/ggy429>
- 639 Hejrani, B., Tkalčić, H., & Fichtner, A. (2017). Centroid moment tensor catalogue using a 3-
640 D continental scale Earth model: Application to earthquakes in Papua New Guinea and
641 the Solomon Islands. *Journal of Geophysical Research: Solid Earth*, 122(7), 5517–5543.
642 <https://doi.org/10.1002/2017JB014230>
- 643 Helffrich, G., Wookey, J., & Bastow, I. (2013). *The Seismic Analysis Code*. Cambridge:
644 Cambridge University Press. <https://doi.org/10.1017/CBO9781139547260>
- 645 Ide, S. (2010). Striations, duration, migration and tidal response in deep tremor. *Nature*,
646 466(7304), 356–359. <https://doi.org/10.1038/nature09251>
- 647 Ide, S., & Maury, J. (2018). Seismic Moment, Seismic Energy, and Source Duration of Slow
648 Earthquakes: Application of Brownian slow earthquake model to three major subduction
649 zones. *Geophysical Research Letters*, 45(7), 3059–3067.

- 650 <https://doi.org/10.1002/2018GL077461>
- 651 Ide, S., & Yabe, S. (2014). Universality of slow earthquakes in the very low frequency band.
652 *Geophysical Research Letters*, *41*(8), 2786–2793.
- 653 <https://doi.org/10.1002/2014GL059712>
- 654 Ide, S., Beroza, G. C., Prejean, S. G., & Ellsworth, W. L. (2003). Apparent break in
655 earthquake scaling due to path and site effects on deep borehole recordings. *Journal of*
656 *Geophysical Research: Solid Earth*, *108*(B5). <https://doi.org/10.1029/2001JB001617>
- 657 Ide, S., Imanishi, K., Yoshida, Y., Beroza, G. C., & Shelly, D. R. (2008). Bridging the gap
658 between seismically and geodetically detected slow earthquakes. *Geophysical Research*
659 *Letters*, *35*(10), 2–7. <https://doi.org/10.1029/2008GL034014>
- 660 Imperatori, W., & Mai, P. M. (2013). Broad-band near-field ground motion simulations in 3-
661 dimensional scattering media. *Geophysical Journal International*, *192*(2), 725–744.
662 <https://doi.org/10.1093/gji/ggs041>
- 663 Imperatori, W., & Mai, P. M. (2015). The role of topography and lateral velocity
664 heterogeneities on near-source scattering and ground-motion variability. *Geophysical*
665 *Journal International*, *202*(3), 2163–2181. <https://doi.org/10.1093/gji/ggv281>
- 666 Iwaki, A., Maeda, T., Morikawa, N., Takemura, S., & Fujiwara, H. (2018). Effects of random
667 3D upper crustal heterogeneity on long-period (≥ 1 s) ground-motion simulations. *Earth,*
668 *Planets and Space*, *70*(1), 156. <https://doi.org/10.1186/s40623-018-0930-5>
- 669 Kanamori, H., & Rivera, L. (2008). Source inversion of W phase: Speeding up seismic
670 tsunami warning. *Geophysical Journal International*, *175*(1), 222–238.
671 <https://doi.org/10.1111/j.1365-246X.2008.03887.x>
- 672 Kaneko, Y., Ito, Y., Chow, B., Wallace, L. M., Tape, C., Grapenthin, R., et al. (2019). Ultra-
673 long Duration of Seismic Ground Motion Arising From a Thick, Low-Velocity
674 Sedimentary Wedge. *Journal of Geophysical Research: Solid Earth*, *124*(10), 10347–
675 10359. <https://doi.org/10.1029/2019JB017795>
- 676 Kano, M., Aso, N., Matsuzawa, T., Ide, S., Annoura, S., Arai, R., et al. (2018). Development
677 of a Slow Earthquake Database. *Seismological Research Letters*, *89*(4), 1566–1575.
678 <https://doi.org/10.1785/0220180021>
- 679 Kao, H., Wang, K., Dragert, H., Kao, J. Y., & Rogers, G. (2010). Estimating seismic moment
680 magnitude (M_w) of tremor bursts in northern Cascadia: Implications for the “seismic
681 efficiency” of episodic tremor and slip. *Geophysical Research Letters*, *37*(19), n/a-n/a.
682 <https://doi.org/10.1029/2010GL044927>
- 683 Kato, A., Obara, K., Igarashi, T., Tsuruoka, H., Nakagawa, S., & Hirata, N. (2012).
684 Propagation of slow slip leading up to the 2011 Mw9.0 Tohoku-Oki earthquake.
685 *Science*, *335*(6069), 705–708. <https://doi.org/10.1126/science.1215141>
- 686 Koketsu, K., Miyake, H., & Suzuki, H. (2012). Japan Integrated Velocity Structure Model
687 Version 1. *Proceedings of the 15th World Conference on Earthquake Engineering*, 1–4.

- 688 Retrieved from http://www.iitk.ac.in/nicee/wcee/article/WCEE2012_1773.pdf
- 689 Kubo, H., Nakamura, T., Suzuki, W., Kimura, T., Kunugi, T., Takahashi, N., & Aoi, S.
690 (2018). Site Amplification Characteristics at Nankai Seafloor Observation Network,
691 DONET1, Japan, Evaluated Using Spectral Inversion. *Bulletin of the Seismological*
692 *Society of America*, XX(Xx), 1–9. <https://doi.org/10.1785/0120170254>
- 693 Kumagai, H., Lacson, R., Maeda, Y., Figueroa, M. S., Yamashina, T., Ruiz, M., et al. (2013).
694 Source amplitudes of volcano-seismic signals determined by the amplitude source
695 location method as a quantitative measure of event size. *Journal of Volcanology and*
696 *Geothermal Research*, 257, 57–71. <https://doi.org/10.1016/j.jvolgeores.2013.03.002>
- 697 Kurokawa, A., Takeo, M., & Kurita, K. (2016). Two types of volcanic tremor changed with
698 eruption style during 1986 Izu-Oshima eruption. *Journal of Geophysical Research:*
699 *Solid Earth*, 121(4), 2727–2736. <https://doi.org/10.1002/2015JB012500>
- 700 Maeda, T., & Obara, K. (2009). Spatiotemporal distribution of seismic energy radiation from
701 low-frequency tremor in western Shikoku, Japan. *Journal of Geophysical Research:*
702 *Solid Earth*, 114(10). <https://doi.org/10.1029/2008JB006043>
- 703 Maeda, T., Takemura, S., & Furumura, T. (2017). OpenSWPC: an open-source integrated
704 parallel simulation code for modeling seismic wave propagation in 3D heterogeneous
705 viscoelastic media. *Earth, Planets and Space*, 69(1), 102.
706 <https://doi.org/10.1186/s40623-017-0687-2>
- 707 Margerin, L. (2005). Introduction to radiative transfer of seismic waves. *Geophysical*
708 *Monograph Series*, 157(January 2005), 229–252. <https://doi.org/10.1029/157GM14>
- 709 Morioka, H., Kumagai, H., & Maeda, T. (2017). Theoretical basis of the amplitude source
710 location method for volcano-seismic signals. *Journal of Geophysical Research: Solid*
711 *Earth*, 122(8), 6538–6551. <https://doi.org/10.1002/2017JB013997>
- 712 Nakahara, H. (2008). Chapter 15 Seismogram Envelope Inversion for High-Frequency
713 Seismic Energy Radiation from Moderate-to-Large Earthquakes. In *Advances in*
714 *Geophysics* (Vol. 50, pp. 401–426). [https://doi.org/10.1016/S0065-2687\(08\)00015-0](https://doi.org/10.1016/S0065-2687(08)00015-0)
- 715 Nakamura, T., Takenaka, H., Okamoto, T., Ohori, M., & Tsuboi, S. (2015). Long-period
716 ocean-bottom motions in the source areas of large subduction earthquakes. *Scientific*
717 *Reports*, 5, 1–2. <https://doi.org/10.1038/srep16648>
- 718 Nakano, M., Kumagai, H., & Inoue, H. (2008). Waveform inversion in the frequency domain
719 for the simultaneous determination of earthquake source mechanism and moment
720 function. *Geophysical Journal International*, 173(3), 1000–1011.
721 <https://doi.org/10.1111/j.1365-246X.2008.03783.x>
- 722 Nakano, M., Nakamura, T., & Kaneda, Y. (2015). Hypocenters in the nankai trough
723 determined by using data from both ocean-bottom and land seismic networks and a 3D
724 velocity structure model: Implications for seismotectonic activity. *Bulletin of the*
725 *Seismological Society of America*, 105(3), 1594–1605.

- 726 <https://doi.org/10.1785/0120140309>
- 727 Nakano, M., Hori, T., Araki, E., Kodaira, S., & Ide, S. (2018). Shallow very-low-frequency
728 earthquakes accompany slow slip events in the Nankai subduction zone. *Nature*
729 *Communications*, 9(1), 984. <https://doi.org/10.1038/s41467-018-03431-5>
- 730 Nakano, M., Hyodo, M., Nakanishi, A., Yamashita, M., Hori, T., Kamiya, S., et al. (2018).
731 The 2016 Mw 5.9 earthquake off the southeastern coast of Mie Prefecture as an
732 indicator of preparatory processes of the next Nankai Trough megathrust earthquake.
733 *Progress in Earth and Planetary Science*, 5(1), 30. [https://doi.org/10.1186/s40645-018-](https://doi.org/10.1186/s40645-018-0188-3)
734 [0188-3](https://doi.org/10.1186/s40645-018-0188-3)
- 735 Nakano, M., Yabe, S., Sugioka, H., Shinohara, M., & Ide, S. (2019). Event Size Distribution
736 of Shallow Tectonic Tremor in the Nankai Trough. *Geophysical Research Letters*,
737 46(11), 5828–5836. <https://doi.org/10.1029/2019GL083029>
- 738 National Research Institute for Earth Science and Disaster Resilience. (2019a). NIED
739 DONET. <https://doi.org/10.17598/NIED.0008>
- 740 National Research Institute for Earth Science and Disaster Resilience. (2019b). NIED F-net.
741 <https://doi.org/10.17598/NIED.0005>
- 742 National Research Institute for Earth Science and Disaster Resilience. (2019c). NIED S-net.
743 <https://doi.org/10.17598/NIED.0007>
- 744 Nishikawa, T., Matsuzawa, T., Ohta, K., Uchida, N., Nishimura, T., & Ide, S. (2019). The
745 slow earthquake spectrum in the Japan Trench illuminated by the S-net seafloor
746 observatories. *Science*, 365(August), 808–813. <https://doi.org/10.1126/science.aax5618>
- 747 Peng, Z., & Zhao, P. (2009). Migration of early aftershocks following the 2004 Parkfield
748 earthquake. *Nature Geoscience*, 2(12), 877–881. <https://doi.org/10.1038/ngeo697>
- 749 Petukhin, A., Miyakoshi, K., Tsurugi, M., Kawase, H., & Kamae, K. (2016). Visualization of
750 Green 's function anomalies for megathrust source in Nankai Trough by reciprocity
751 method. *Earth, Planets and Space*. <https://doi.org/10.1186/s40623-016-0385-5>
- 752 Poiata, N., Vilotte, J.-P., Bernard, P., Satriano, C., & Obara, K. (2018). Imaging different
753 components of a tectonic tremor sequence in southwestern Japan using an automatic
754 statistical detection and location method. *Geophysical Journal International*, (February).
755 <https://doi.org/10.1093/gji/ggy070/4898035>
- 756 Saito, T., Sato, H., & Ohtake, M. (2002). Envelope broadening of spherically outgoing waves
757 in three-dimensional random media having power law spectra. *Journal of Geophysical*
758 *Research*, 107(B5), 2089. <https://doi.org/10.1029/2001JB000264>
- 759 Saito, T., Sato, H., Ohtake, M., & Obara, K. (2005). Unified explanation of envelope
760 broadening and maximum-amplitude decay high-frequency seismograms based on the
761 envelope simulation using the Markov approximation: Forearc side of the volcanic front
762 in northeastern Honshu, Japan. *Journal of Geophysical Research B: Solid Earth*, 110(1),
763 1–18. <https://doi.org/10.1029/2004JB003225>

- 764 Sato, H., & Emoto, K. (2018). Synthesis of a Scalar Wavelet Intensity Propagating Through
765 von Kármán-type Random Media: Radiative Transfer Theory Using the Born and Phase-
766 Screen Approximations. *Geophysical Journal International*, 909–923.
767 <https://doi.org/10.1093/gji/ggy319>
- 768 Sato, H., Fehler, M. C., & Maeda, T. (2012). Seismic Wave Propagation and Scattering in the
769 Heterogeneous Earth : Second Edition. In *Seismic Wave Propagation and Scattering in*
770 *the Heterogeneous Earth : Second Edition*. Berlin, Heidelberg: Springer Berlin
771 Heidelberg. https://doi.org/10.1007/978-3-642-23029-5_2
- 772 Sawazaki, K., & Enescu, B. (2014). Imaging the high-frequency energy radiation process of a
773 main shock and its early aftershock sequence: The case of the 2008 Iwate-Miyagi
774 Nairiku earthquake, Japan. *Journal of Geophysical Research: Solid Earth*, 119(6),
775 4729–4746. <https://doi.org/10.1002/2013JB010539>
- 776 Shapiro, N. M., Campillo, M., Singh, S. K., & Pacheco, J. (1998). Seismic channel waves in
777 the accretionary prism of the Middle America Trench. *Geophysical Research Letters*,
778 25(1), 101–104. <https://doi.org/10.1029/97GL03492>
- 779 Shapiro, N. M., Olsen, K. B., & Singh, S. K. (2000). Wave-guide effects in subduction zones:
780 Evidence from three-dimensional modeling. *Geophysical Research Letters*, 27(3), 433–
781 436. <https://doi.org/10.1029/1999GL010982>
- 782 Staudenmaier, N., Edwards, B., Tormann, T., Zechar, J. D., & Wiemer, S. (2016). Spatial
783 distribution and energy release of nonvolcanic tremor at Parkfield, California. *Journal of*
784 *Geophysical Research: Solid Earth*, 121(12), 8833–8854.
785 <https://doi.org/10.1002/2016JB013283>
- 786 Supino, M., Poiata, N., Festa, G., Vilotte, J. P., Satriano, C., & Obara, K. (2020). Self-
787 similarity of low-frequency earthquakes. *Scientific Reports*, 10(1), 6523.
788 <https://doi.org/10.1038/s41598-020-63584-6>
- 789 Takahashi, T., Sato, H., Nishimura, T., & Obara, K. (2007). Strong inhomogeneity beneath
790 quaternary volcanoes revealed from the peak delay analysis of S-wave seismograms of
791 microearthquakes in northeastern Japan. *Geophysical Journal International*, 168(1), 90–
792 99. <https://doi.org/10.1111/j.1365-246X.2006.03197.x>
- 793 Takahashi, T., Sato, H., Nishimura, T., & Obara, K. (2009). Tomographic inversion of the
794 peak delay times to reveal random velocity fluctuations in the lithosphere: Method and
795 application to northeastern Japan. *Geophysical Journal International*, 178(3), 1437–
796 1455. <https://doi.org/10.1111/j.1365-246X.2009.04227.x>
- 797 Takemura, S., & Yoshimoto, K. (2014). Strong seismic wave scattering in the low-velocity
798 anomaly associated with subduction of oceanic plate. *Geophysical Journal*
799 *International*, 197(2), 1016–1032. <https://doi.org/10.1093/gji/ggu031>
- 800 Takemura, S., Furumura, T., & Saito, T. (2009). Distortion of the apparent S -wave radiation
801 pattern in the high-frequency wavefield: Tottori-Ken Seibu, Japan, earthquake of 2000.

- 802 *Geophysical Journal International*, 178(2), 950–961. <https://doi.org/10.1111/j.1365->
803 246X.2009.04210.x
- 804 Takemura, S., Furumura, T., & Maeda, T. (2015). Scattering of high-frequency seismic
805 waves caused by irregular surface topography and small-scale velocity inhomogeneity.
806 *Geophysical Journal International*, 201(1), 459–474. <https://doi.org/10.1093/gji/ggv038>
- 807 Takemura, S., Kobayashi, M., & Yoshimoto, K. (2016). Prediction of maximum P- and S-
808 wave amplitude distributions incorporating frequency- and distance-dependent
809 characteristics of the observed apparent radiation patterns. *Earth, Planets and Space*,
810 68(1), 166. <https://doi.org/10.1186/s40623-016-0544-8>
- 811 Takemura, S., Kobayashi, M., & Yoshimoto, K. (2017). High-frequency seismic wave
812 propagation within the heterogeneous crust: effects of seismic scattering and intrinsic
813 attenuation on ground motion modelling. *Geophysical Journal International*, 210(3),
814 1806–1822. <https://doi.org/10.1093/gji/ggx269>
- 815 Takemura, S., Okuwaki, R., Kubota, T., Shiomi, K., Kimura, T., & Noda, A. (2019). Centroid
816 moment tensor inversions of offshore earthquakes using a three-dimensional velocity
817 structure model: Slip distributions on the plate boundary along the Nankai Trough.
818 *EarthArXiv*. <https://doi.org/10.31223/osf.io/nbd79>
- 819 Takemura, S., Kubo, H., Tonegawa, T., Saito, T., & Shiomi, K. (2019). Modeling of Long-
820 Period Ground Motions in the Nankai Subduction Zone: Model Simulation Using the
821 Accretionary Prism Derived from Oceanfloor Local S-Wave Velocity Structures. *Pure
822 and Applied Geophysics*, 176(2), 627–647. <https://doi.org/10.1007/s00024-018-2013-8>
- 823 Takemura, Shunsuke, Shiomi, K., Kimura, T., & Saito, T. (2016). Systematic difference
824 between first-motion and waveform-inversion solutions for shallow offshore
825 earthquakes due to a low-angle dipping slab. *Earth, Planets and Space*, 68(1), 149.
826 <https://doi.org/10.1186/s40623-016-0527-9>
- 827 Takemura, Shunsuke, Matsuzawa, T., Noda, A., Tonegawa, T., Asano, Y., Kimura, T., &
828 Shiomi, K. (2019). Structural Characteristics of the Nankai Trough Shallow Plate
829 Boundary Inferred From Shallow Very Low Frequency Earthquakes. *Geophysical
830 Research Letters*, 46(8), 4192–4201. <https://doi.org/10.1029/2019GL082448>
- 831 Tamaribuchi, K., Kobayashi, A., Nishimiya, T., Hirose, F., & Annoura, S. (2019).
832 Characteristics of shallow low-frequency earthquakes off the Kii Peninsula, Japan, in
833 2004 revealed by ocean bottom seismometers. *Geophysical Research Letters*,
834 2019GL085158. <https://doi.org/10.1029/2019GL085158>
- 835 Tanaka, S., Matsuzawa, T., & Asano, Y. (2019). Shallow Low-Frequency Tremor in the
836 Northern Japan Trench Subduction Zone. *Geophysical Research Letters*, 46(10), 5217–
837 5224. <https://doi.org/10.1029/2019GL082817>
- 838 Thomas, A. M., Beroza, G. C., & Shelly, D. R. (2016). Constraints on the source parameters
839 of low-frequency earthquakes on the San Andreas Fault. *Geophysical Research Letters*,

- 840 43(4), 1464–1471. <https://doi.org/10.1002/2015GL067173>
- 841 Toh, A., Obana, K., & Araki, E. (2018). Distribution of very low frequency earthquakes in
842 the Nankai accretionary prism influenced by a subducting-ridge. *Earth and Planetary*
843 *Science Letters*, 482(March 2011), 342–356. <https://doi.org/10.1016/j.epsl.2017.10.062>
- 844 Tonegawa, T., Fukao, Y., Fujie, G., Takemura, S., Takahashi, T., & Kodaira, S. (2015).
845 Geographical distribution of shear wave anisotropy within marine sediments in the
846 northwestern Pacific. *Progress in Earth and Planetary Science*, 2(1), 27.
847 <https://doi.org/10.1186/s40645-015-0057-2>
- 848 Tonegawa, T., Araki, E., Kimura, T., Nakamura, T., Nakano, M., & Suzuki, K. (2017).
849 Sporadic low-velocity volumes spatially correlate with shallow very low frequency
850 earthquake clusters. *Nature Communications*, 8(1), 2048.
851 <https://doi.org/10.1038/s41467-017-02276-8>
- 852 Tripathi, J. N., Sato, H., & Yamamoto, M. (2010). Envelope broadening characteristics of
853 crustal earthquakes in northeastern Honshu, Japan. *Geophysical Journal International*,
854 182(2), 988–1000. <https://doi.org/10.1111/j.1365-246X.2010.04657.x>
- 855 Uchide, T., & Ide, S. (2010). Scaling of earthquake rupture growth in the Parkfield area: Self-
856 similar growth and suppression by the finite seismogenic layer. *Journal of Geophysical*
857 *Research: Solid Earth*, 115(11), 1–15. <https://doi.org/10.1029/2009JB007122>
- 858 Volk, O., Shani-kadmiel, S., Gvirtzman, Z., & Tsesarsky, M. (2017). 3D Effects of
859 Sedimentary Wedges and Subsurface Canyons : Ground-Motion Amplification in the
860 Israeli Coastal Plain, 107(3). <https://doi.org/10.1785/0120160349>
- 861 Wallace, L. M., Araki, E., Saffer, D., Wang, X., Roesner, A., Kopf, A., et al. (2016). Near-
862 field observations of an offshore M w 6.0 earthquake from an integrated seafloor and
863 subseafloor monitoring network at the Nankai Trough, southwest Japan. *Journal of*
864 *Geophysical Research: Solid Earth*, 121(11), 8338–8351.
865 <https://doi.org/10.1002/2016JB013417>
- 866 Wang, X., & Zhan, Z. (2020). Moving from 1-D to 3-D velocity model: automated
867 waveform-based earthquake moment tensor inversion in the Los Angeles region.
868 *Geophysical Journal International*, 220(1), 218–234. <https://doi.org/10.1093/gji/ggz435>
- 869 Wegler, U., Korn, M., & Przybilla, J. (2006). Modeling Full Seismogram Envelopes Using
870 Radiative Transfer Theory with Born Scattering Coefficients. *Pure and Applied*
871 *Geophysics*, 163(2–3), 503–531. <https://doi.org/10.1007/s00024-005-0027-5>
- 872 Wessel, P., Smith, W. H. F., Scharroo, R., Luis, J., & Wobbe, F. (2013). Generic mapping
873 tools: Improved version released. *Eos*, 94(45), 409–410.
874 <https://doi.org/10.1002/2013EO450001>
- 875 Yabe, S., & Ide, S. (2014). Spatial distribution of seismic energy rate of tectonic tremors in
876 subduction zones. *Journal of Geophysical Research: Solid Earth*, 119(11), 8171–8185.
877 <https://doi.org/10.1002/2014JB011383>

- 878 Yabe, S., Tonegawa, T., & Nakano, M. (2019). Scaled Energy Estimation for Shallow Slow
879 Earthquakes. *Journal of Geophysical Research: Solid Earth*, *124*(2), 1507–1519.
880 <https://doi.org/10.1029/2018JB016815>
- 881 Yoshimoto, K., Takemura, S., & Kobayashi, M. (2015). Application of scattering theory to P-
882 wave amplitude fluctuations in the crust. *Earth, Planets and Space*, *67*(1), 199.
883 <https://doi.org/10.1186/s40623-015-0366-0>
- 884 Zhang, W., & Shen, Y. (2010). Unsplit complex frequency-shifted PML implementation
885 using auxiliary differential equations for seismic wave modeling. *GEOPHYSICS*, *75*(4),
886 T141–T154. <https://doi.org/10.1190/1.3463431>
- 887

1 **Supporting information:**

2 **Modelling high-frequency seismograms at ocean bottom seismometers:**
3 **effects of heterogeneous structures on source parameter estimation of small**
4 **offshore earthquakes and shallow low-frequency tremors**

5
6 **Authors**

7 **Shunsuke TAKEMURA^{1*}, Suguru YABE², Kentaro EMOTO³**

8 ¹**Earthquake Research Institute, the University of Tokyo, 1-1-1 Yayoi, Bunkyo-ku,**
9 **Tokyo, 113-0032, Japan**

10 ²**Geological Survey of Japan, National Institute of Advanced Industrial Science and**
11 **Technology, Tsukuba Central 7, 1-1-1 Higashi, Tsukuba, Ibaraki, 305-8567, Japan**

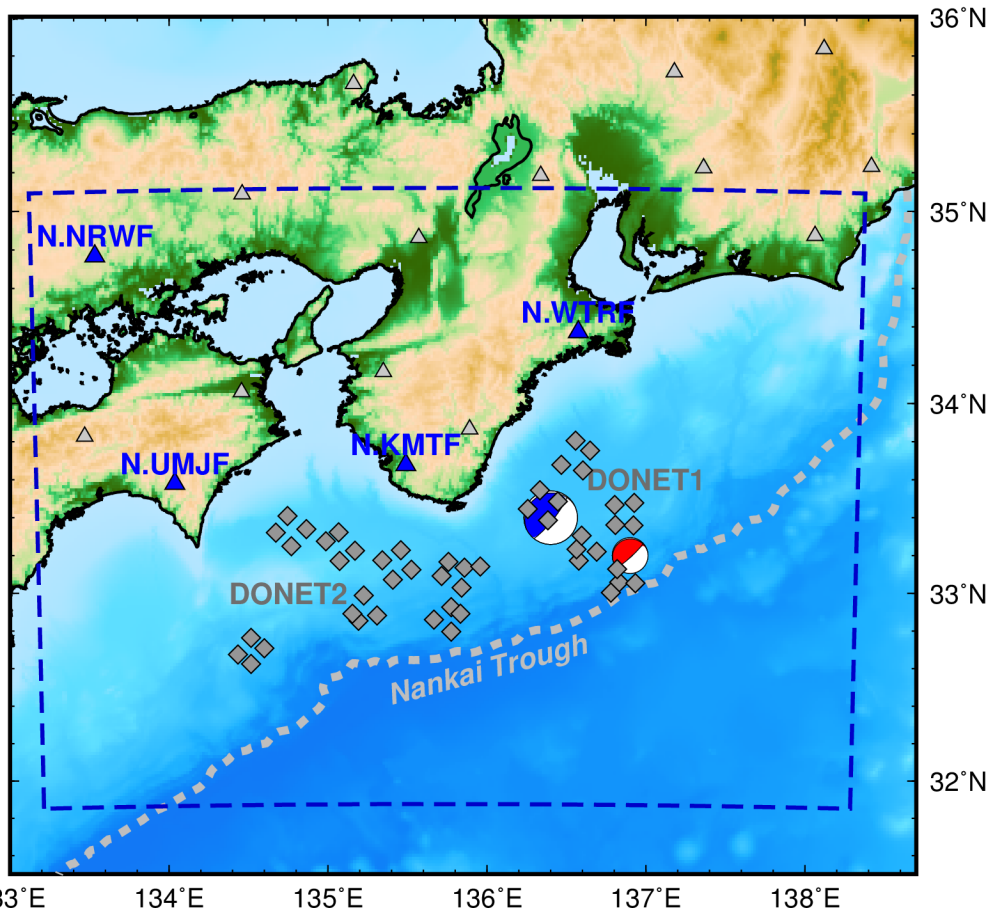
12 ³**Geophysics, Graduate School of Science, Tohoku University, 6-3, Aramaki-aza-**
13 **aoba, Aoba-ku, Sendai, 980-8578, Japan**

14
15 **Text S1**

16 The 3D model used in the simulations was basically constructed from the Japan Integrated
17 Velocity Structure Model (JIVSM) (Koketsu *et al.* 2012). Because the accretionary prism of
18 the JIVSM is modelled by a $V_S = 1$ km/s constant layer and is too simple for realistic ground
19 motion simulation, we introduced estimations of 1D S -wave velocity structures beneath
20 DONET stations by Tonegawa *et al.* (2017). We converted the depth-varying velocity structure
21 model of Tonegawa *et al.* (2017) to a 5-layer model beneath each DONET station. The physical
22 parameters of each layer are listed in Table 1 of the main text. Thicknesses of each layer were
23 determined by fitting the depth-average S -wave velocities derived by Tonegawa *et al.* (2017).
24 For example, if the depth-average V_S of Tonegawa *et al.* (2017) become the V_S of layer 1 at a
25 certain depth, this depth is considered as the bottom of layer 1. After obtaining the bottom
26 depths of layers 1–4 beneath DONET stations, the bottom depths of each station were
27 interpolated and extrapolated via the ‘*Surface*’ gridding algorithm in Generic Mapping Tools
28 software (GMT; Wessel *et al.* 2013). Interpolation and extrapolation were only applied within
29 the region of the accretionary prism. In other words, the JIVSM onshore and outer-rise
30 sedimentary structures, and structures beneath bedrock, were fixed.

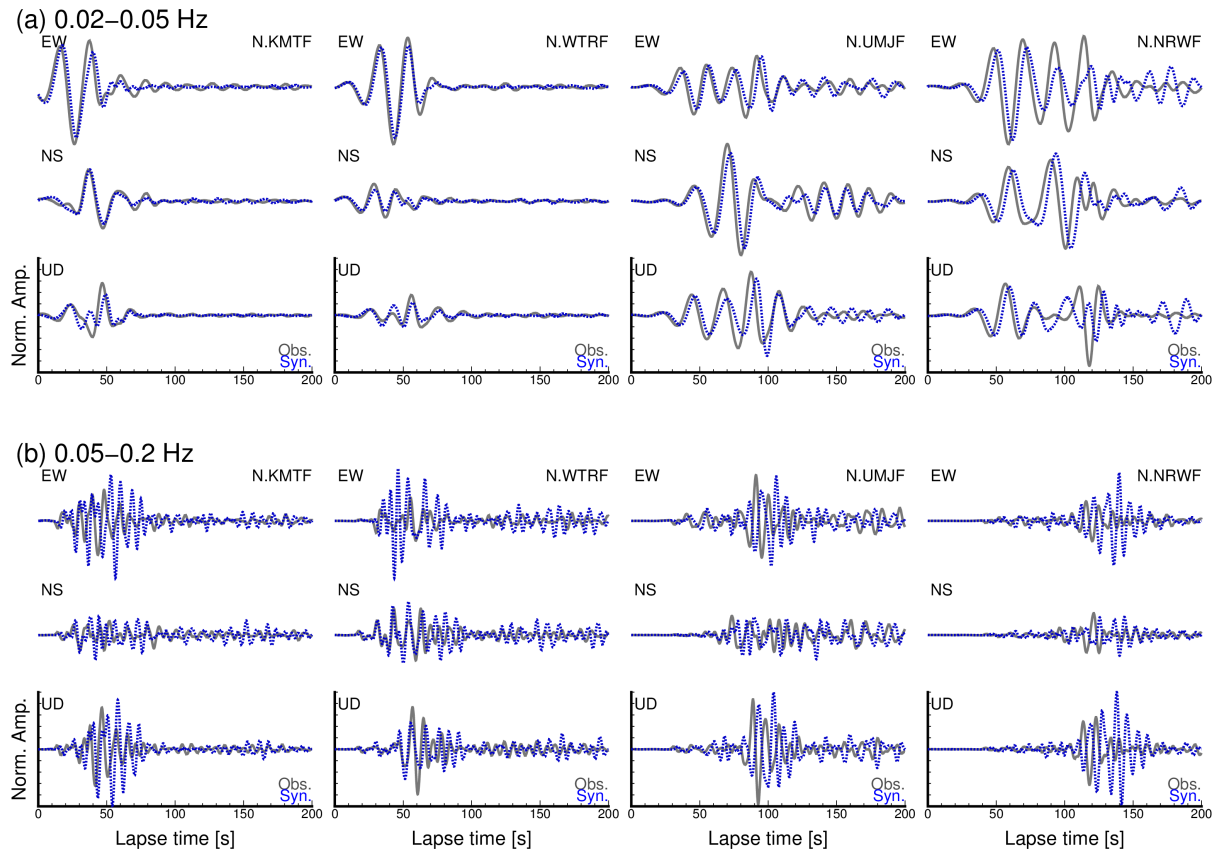
31 This construction method was basically the same as in Takemura, Kubo, *et al.* (2019).
32 However, in the present model, a layered structure was employed rather than a depth velocity-
33 gradient function. The simulation results of both the smooth-gradient and layered models were

34 almost the same (Figures S1–S3).



35 133°E 134°E 135°E 136°E 137°E 138°E
36 **Figure S1.** Map for validation of simulations. The dashed-blue rectangle represents the
37 horizontal coverage of the calculation region, which was discretised at intervals of 0.2
38 km in horizontal directions and 0.1 km in the vertical direction. Simulations were
39 conducted using the computer system at the Earthquake and Volcano Information Center,
40 Earthquake Research Institute, University of Tokyo. The blue and red focal spheres are
41 CMT solutions of the 2016 M_w 5.9 earthquake southeast off Kii Peninsula, Japan
42 (Takemura, Okuwaki, *et al.* 2019), and a shallow very low-frequency earthquake on 10
43 April 2016 (Takemura *et al.* 2018, Takemura, Matsuzawa, *et al.* 2019), respectively. The
44 triangles and diamonds represent F-net and DONET stations, respectively.

45
46



47

48

Figure S2. Simulation of the 2016 M_w 5.9 earthquake southeast off Kii Peninsula, Japan

49

(Takemura, Okuwaki, *et al.* 2019): (a) 0.02–0.05 Hz, (b) 0.05–0.2 Hz. Seismic wave

50

propagation in our model was evaluated via OpenSWPC software (Maeda *et al.* 2017).

51

The simulation model covered the area within the blue rectangle shown in Figure S1,

52

which was discretised by grid intervals of 0.2 km in horizontal directions and 0.1 km in

53

the vertical direction. Observed and synthetic seismograms at F-net stations are

54

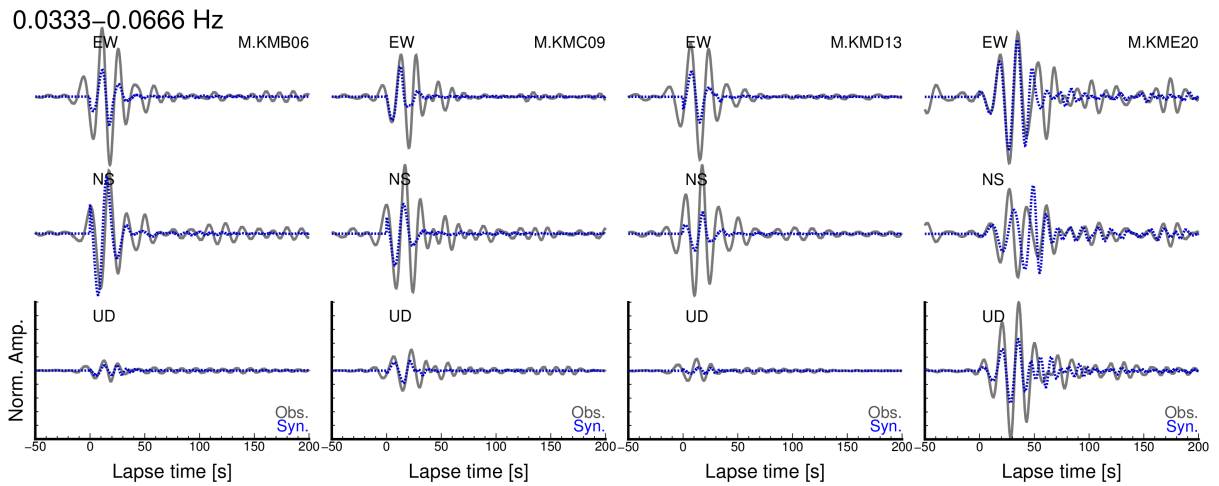
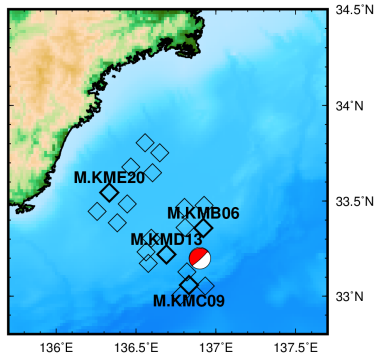
represented by grey and blue dotted lines, respectively. Amplitudes at each station were

55

normalized by the maximum amplitude of six-component filtered seismograms.

56

57

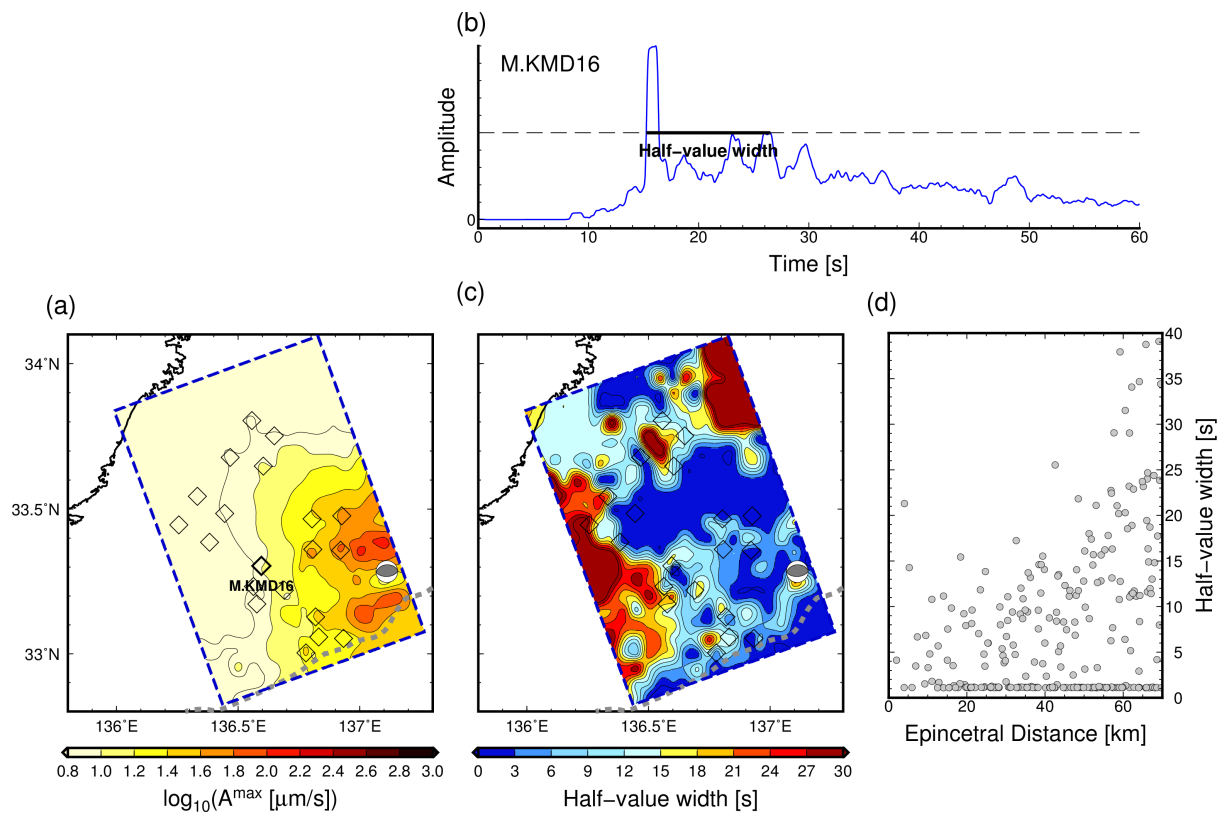


58

59 **Figure S3.** Simulation result of a shallow very low-frequency earthquake on 10 April 2016
 60 (Takemura *et al.* 2018, Takemura, Matsuzawa, *et al.* 2019). Observed and synthetic
 61 seismograms at DONET stations are represented by grey and blue dotted lines,
 62 respectively. Amplitudes at each station were normalized by the maximum amplitude of
 63 six-component filtered seismograms. Locations of stations and the source are shown in
 64 the upper-left panel. The simulation model and settings are similar to those in Figure S2.

65

66

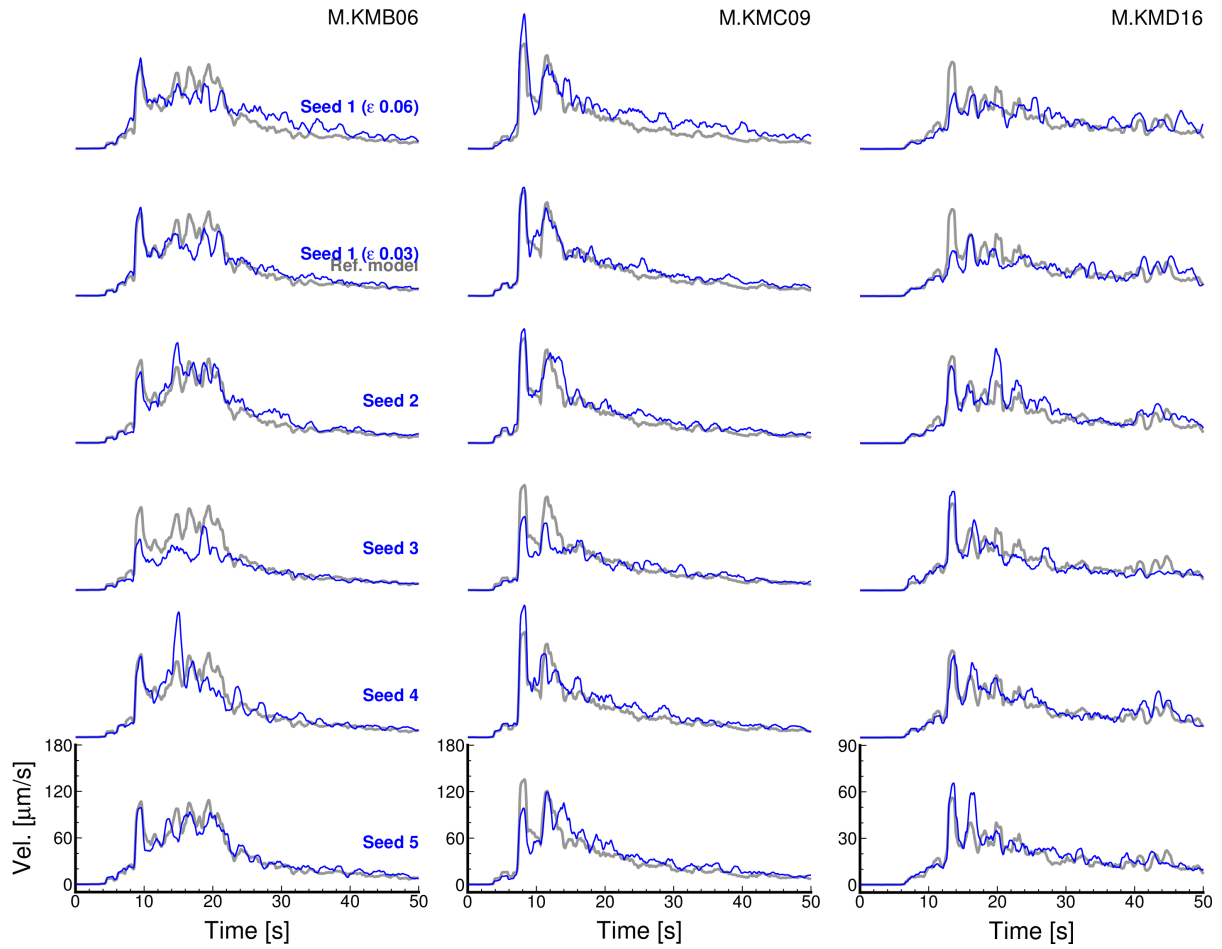


67

68 **Figure S4.** Spatial variations of maximum RMS amplitudes and half-value widths of
 69 simulated RMS envelopes for an intraslab earthquake: (a) Maximum RMS amplitude
 70 distribution, (b) example half-value width estimations, (c) half-value width distribution,
 71 and (d) half-value widths as a function of epicentral distance. An example in (b) is an
 72 RMS envelope at M.MRD16 (location shown in (a)).

73

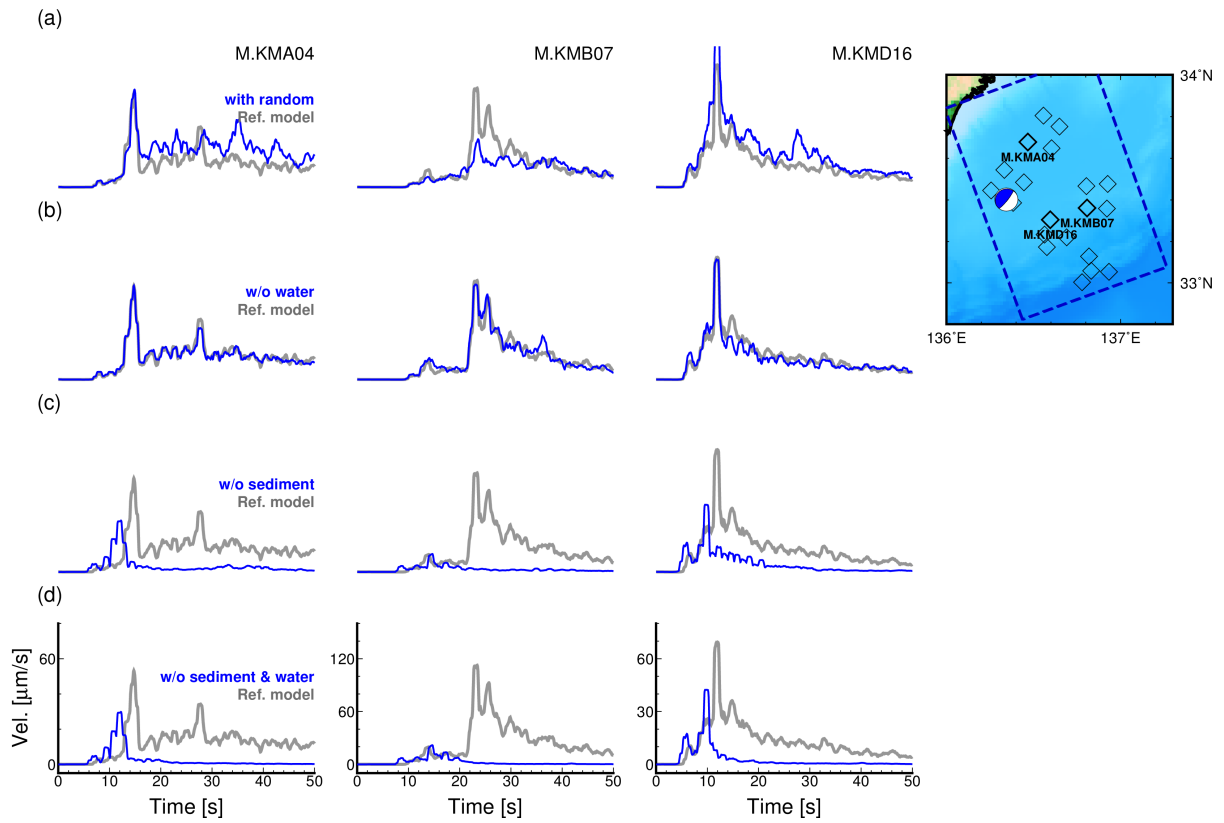
74



75

76 **Figure S5.** Comparisons of simulated RMS envelopes with different small-scale random
 77 velocity heterogeneity models. The PSDF type is an exponential type, and the parameters
 78 for small-scale random velocity heterogeneity models within the crust and accretionary
 79 prism are correlation length of $a = 1$ km and RMS values of $\varepsilon = 0.03, 0.06$. The models
 80 with $a = 1$ km and $\varepsilon = 0.03$ were conducted using different random seeds (numbered 1–
 81 5). Details of small-scale velocity heterogeneity models are described in Table 3.
 82 Locations of DONET stations are shown in Figure 8.

83



84

85 **Figure S6.** Simulation results of various heterogeneous models for an interplate earthquake.

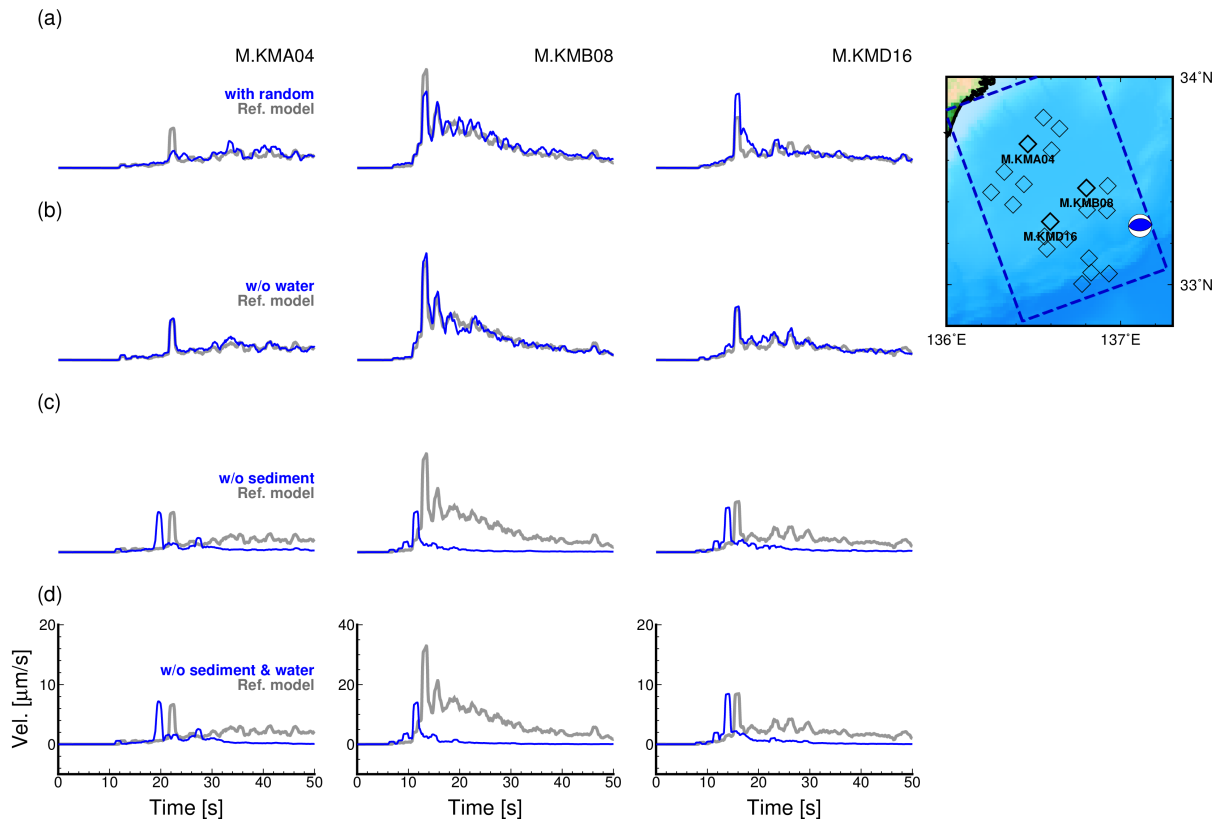
86 The blue lines are RMS envelopes derived from models: (a) with small-scale random

87 velocity heterogeneities, (b) without seawater, (c) without oceanic sediments

88 (accretionary prism), and (d) without oceanic sediments and seawater. Grey lines are the

89 simulation results with the reference model.

90



91

92 **Figure S7.** Simulation results of various heterogeneous models for an intraslab earthquake.

93 The blue lines are RMS envelopes derived from models: (a) with small-scale random

94 velocity heterogeneities, (b) without seawater, (c) without oceanic sediments

95 (accretionary prism), and (d) without oceanic sediments and seawater. Grey lines are the

96 simulation results with the reference model.

97

98 **References**

- 99 Koketsu, K., Miyake, H. & Suzuki, H. (2012) Japan Integrated Velocity Structure Model
100 Version 1. *Proc. 15th World Conf. Earthq. Eng.*, 1–4. Retrieved from
101 http://www.iitk.ac.in/nicee/wcee/article/WCEE2012_1773.pdf
- 102 Maeda, T., Takemura, S. & Furumura, T. (2017) OpenSWPC: an open-source integrated
103 parallel simulation code for modeling seismic wave propagation in 3D heterogeneous
104 viscoelastic media. *Earth, Planets Sp.*, **69**, 102, Springer Berlin Heidelberg.
105 doi:10.1186/s40623-017-0687-2
- 106 Takemura, S., Kubo, H., Tonegawa, T., Saito, T. & Shiomi, K. (2019) Modeling of Long-
107 Period Ground Motions in the Nankai Subduction Zone: Model Simulation Using the
108 Accretionary Prism Derived from Oceanfloor Local S-Wave Velocity Structures. *Pure
109 Appl. Geophys.*, **176**, 627–647, Birkhauser Verlag AG. doi:10.1007/s00024-018-2013-8
- 110 Takemura, S., Matsuzawa, T., Kimura, T., Tonegawa, T. & Shiomi, K. (2018) Centroid
111 moment tensor inversion of shallow very low-frequency earthquakes off the Kii
112 Peninsula, Japan, using a three-dimensional velocity structure model. *Geophys. Res.
113 Lett.*, **45**, 6450–6458. doi:10.1029/2018GL078455
- 114 Takemura, S., Matsuzawa, T., Noda, A., Tonegawa, T., Asano, Y., Kimura, T. & Shiomi, K.
115 (2019) Structural Characteristics of the Nankai Trough Shallow Plate Boundary Inferred
116 From Shallow Very Low Frequency Earthquakes. *Geophys. Res. Lett.*, **46**, 4192–4201,
117 Blackwell Publishing Ltd. doi:10.1029/2019GL082448
- 118 Takemura, S., Okuwaki, R., Kubota, T., Shiomi, K., Kimura, T. & Noda, A. (2019) Centroid
119 moment tensor inversions of offshore earthquakes using a three- dimensional velocity
120 structure model : Slip distributions on the plate boundary along the Nankai Trough.
121 *EarthArXiv*. doi:10.31223/osf.io/nbd79
- 122 Tonegawa, T., Araki, E., Kimura, T., Nakamura, T., Nakano, M. & Suzuki, K. (2017)
123 Sporadic low-velocity volumes spatially correlate with shallow very low frequency
124 earthquake clusters. *Nat. Commun.*, **8**, 2048. doi:10.1038/s41467-017-02276-8
125